



HAL
open science

Structure of birnessite obtained from decomposition of permanganate under soft hydrothermal conditions. I. Chemical and structural evolution as a function of temperature.

Anne-Claire Gaillot, Bruno Lanson, Victor A. Drits

► **To cite this version:**

Anne-Claire Gaillot, Bruno Lanson, Victor A. Drits. Structure of birnessite obtained from decomposition of permanganate under soft hydrothermal conditions. I. Chemical and structural evolution as a function of temperature.. *Chemistry of Materials*, 2005, 17 (11), pp.2959-2975. 10.1021/cm0500152 . hal-00106999

HAL Id: hal-00106999

<https://hal.science/hal-00106999>

Submitted on 17 Oct 2006

HAL is a multi-disciplinary open access archive for the deposit and dissemination of scientific research documents, whether they are published or not. The documents may come from teaching and research institutions in France or abroad, or from public or private research centers.

L'archive ouverte pluridisciplinaire **HAL**, est destinée au dépôt et à la diffusion de documents scientifiques de niveau recherche, publiés ou non, émanant des établissements d'enseignement et de recherche français ou étrangers, des laboratoires publics ou privés.

**Structure of birnessite obtained from decomposition of permanganate
under soft hydrothermal conditions. I. Chemical and structural
evolution as a function of temperature**

Anne-Claire Gaillot¹

Bruno Lanson^{1,*}

Victor A. Drits^{1,2}

1 – Environmental Geochemistry Group, LGIT – Maison des Géosciences, University of Grenoble – CNRS, 38041 Grenoble Cedex 9, France.

2 – Geological Institute, Russian Academy of Sciences, 7 Pyzhevsky street, 109017 Moscow, Russia

* Author to whom correspondence should be addressed.

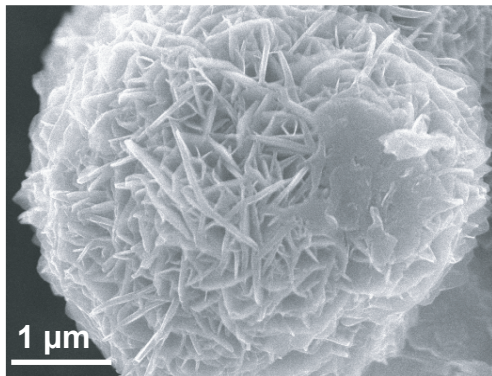
e-mail: Bruno.Lanson@obs.ujf-grenoble.fr

For Table of Contents Use Only

Structure of birnessite obtained from decomposition of permanganate under soft hydrothermal conditions. I. Chemical and structural evolution as a function of temperature

Anne-Claire Gaillot, Bruno Lanson, Victor A. Drits

Layers of hydrothermally synthesized birnessite are exclusively built up of Mn^{4+} octahedra and the layer charge deficit arises solely from the presence of vacant layer sites. When heated to 350°C , layer Mn^{4+} cations are partially reduced to Mn^{3+} , leading to the departure of O_{layer} atoms. After cooling, layer symmetry is lowered from hexagonal to orthogonal as the result of the segregation of Mn^{3+} -octahedra in rows parallel to the **b** axis and by the systematic orientation of their long Mn-O bonds along the **a** axis.



Abstract

The structure of a synthetic K-rich birnessite (KBi) prepared by hydrothermally reacting (4 days at 170°C) a finely ground KMnO_4 powder in acidified water was determined. At room temperature the structure of KBi corresponds to a $3R^-$ polytype which can be described as $\text{AbC}_b^a \text{CaB}_c^a \text{BcA}_b^c \text{AbC} \dots$ using the close-packing formalism. Assuming an orthogonal base-centered unit cell, KBi has $a = b\sqrt{3} = 4.923 \text{ \AA}$, $b = 2.845 \text{ \AA}$, $\gamma = 90^\circ$ and $c = 21.492 \text{ \AA}$. The layer charge deficit originates exclusively from the presence of vacant layer sites as only Mn^{4+} cations are present in the octahedral layers, and the following structural formula can be proposed: $\text{K}_{0.296}^+ (\text{Mn}_{0.926}^{4+} \square_{0.074}) \text{O}_2 \cdot 0.40 \text{H}_2\text{O}$. The layer charge deficit is compensated by the sole presence of interlayer K in prismatic cavities located above (or below) an empty tridentate cavity of the lower (or upper) layer and below (or above) a Mn octahedron of the upper (or lower) layer. This site is shifted from the center of the prismatic cavity towards its faces. This structure is essentially unaffected when heating this sample up to 250°C, except for the dehydration of KBi interlayers.

Heating the KBi sample to 350°C leads to a dramatic modification of its crystal chemistry resulting from the partial reduction of layer Mn^{4+} cations associated with the departure of O_{layer} atoms. In spite of unfavorable steric strains induced by the Jahn-Teller distortion of Mn^{3+} octahedra, reduced Mn^{3+} cations remain in the octahedral layers leading to vacancy-free layers with the following structural formula: $\text{K}_{0.312}^+ (\text{Mn}_{0.761}^{4+} \text{Mn}_{0.215}^{3+} \square_{0.024}) \text{O}_2 \cdot 0.42 \text{H}_2\text{O}$. At 350°C the partial reduction of Mn_{layer} leads to dramatic increase of the lateral dimensions of the layer arising from the random orientation of the long $\text{Mn}^{3+}\text{-O}$ bond with respect to the **a** axis. After cooling, the structure of KBi becomes monoclinic (space group $C2/m$) with $a = 5.130 \text{ \AA}$, $b = 2.850 \text{ \AA}$, $c = 7.131 \text{ \AA}$, $\beta = 101.0^\circ$. In this case steric strains are minimized by the segregation of Mn^{3+} -octahedra in

26 Mn³⁺-rich rows parallel to the **b** axis and by the systematic orientation of their long Mn-O
27 bonds along the **a** axis.

28 The origin of the above structural modifications and the nature of the stacking disorder
29 are also determined.

30

31 **Introduction**

32

33 Birnessite has a layer structure consisting of edge-sharing MnO₆ octahedra with hydrated
34 cations in the interlayer space compensating for the layer charge deficit which arises either
35 from the coexistence of heterovalent Mn cations within layers or from the presence of vacant
36 layer octahedra.¹⁻⁵ This mineral occurs in diverse geological settings including deep-ocean
37 nodules, ore deposits of Mn and other metals, soils and alteration crusts.³⁻¹⁹ Although present
38 in limited amounts, birnessite plays a pivotal role in the fate of heavy metals and other
39 pollutants in contaminated water systems and soils.¹⁸⁻³¹ This role originates from its unique
40 cation exchange capacity,³²⁻³⁶ sorption,³⁶⁻⁴⁸ and redox properties.^{21,28,36,45-54}

41 To study these properties and the reaction mechanisms involved, synthetic birnessite-like
42 structures are most often used as they are easily obtained under laboratory conditions.
43 Recently, synthetic birnessite has attracted additional attention as a potential cathode material
44 for rechargeable batteries, and extensive research is presently carried out to define optimal
45 conditions for the synthesis of a low-cost and environmentally-safe birnessite-like structure to
46 replace the LiCoO₂ cathode commonly used in commercial cells. Birnessite is synthesized
47 either from the oxidation of Mn²⁺ in a highly alkaline medium,^{1,2,10,55} or from the reduction of
48 Mn⁷⁺ using permanganate (MnO₄⁻) as starting reagent. In the latter case, different protocols
49 have been proposed including mild hydrothermal synthesis,⁵⁶⁻⁵⁸ sol-gel processes,⁵⁹⁻⁶⁴,
50 interaction of KMnO₄ with hydrochloric acid followed by a cation exchange,^{7,65-67} and

51 thermal decomposition of KMnO_4 or of a MnO-LiOH-KNO_3 mixture at very high
52 temperatures.^{55,68-70}

53 Birnessites obtained by these protocols differ from each other by important structural and
54 chemical features and by their properties. Therefore, to understand the relationships between
55 structure and properties of the different birnessite varieties a comprehensive crystal chemical
56 study of each variety is required. In the present article and in the companion article structural
57 and chemical features of birnessite samples obtained from the mild hydrothermal treatment of
58 potassium and sodium permanganates are investigated.⁷¹ From the decomposition at 170°C of
59 KMnO_4 in acidified water this synthesis protocol initially developed by Chen et al. directly
60 leads to a K-birnessite variety with structural formula $\text{K}_{0.25}\text{MnO}_2 \cdot 0.6\text{H}_2\text{O}$.^{57,58} These authors
61 concluded that this birnessite variety has a hexagonal layer symmetry, a three-layer
62 periodicity, and crystallizes in space group $R\bar{3}m$. Using the integrated intensity refinement
63 approach they also determined an idealized structure model for this K-birnessite variety.⁵⁷
64 However, important details of the actual structure of this hydrothermally synthesized
65 birnessite variety were only partially determined. In particular, atomic positions of the
66 different interlayer species (K^+ cations and H_2O molecules) were not differentiated. More
67 important, the average oxidation degree of Mn and the origin of the layer charge (coexistence
68 of heterovalent Mn cations and/or presence of vacant layer sites) were not determined. In
69 addition, these authors recognized that important issues such as the nature of structural
70 defects in these phylломanganates needed to be refined. These structural features of K-
71 birnessite are specifically detailed in the present manuscript. In addition, special attention is
72 paid to the structural modifications observed as a function of temperature. Structural
73 modifications of K-birnessite resulting from cation exchange processes are described in the
74 companion paper.⁷¹

75

76

Experimental Section

77

78 **Experimental Methods.** K-birnessite (hereafter referred to as KBi) was prepared by
79 acidifying 0.025 mol of finely ground KMnO_4 in 50 mL of water with 5 drops of 4M HNO_3
80 giving a pH of ~ 3 and a $\text{Mn}:\text{H}^+$ ratio of 100:1.⁵⁷ After aging for one month in a light-free
81 environment and under constant stirring, the solution was transferred into a 250 mL Teflon-
82 lined autoclave (Paar bomb), sealed, and reacted hydrothermally for four days at 170°C .
83 After reaction, the solution pH was highly alkaline (pH ~ 13). The resulting black crystals
84 were filtered, washed several times with deionized Milli-Q water ($18.2 \text{ M}\Omega\cdot\text{cm}^{-1}$), then
85 freeze-dried and stored under room conditions for further chemical and structural
86 characterizations.

87 The morphology of KBi particles was observed on a JEOL JSM 6320F high-resolution
88 scanning electron microscope (SEM) equipped with a field-emission electron source.

89 **Thermal and Chemical Analyses – Structural Formula.** Thermal analysis of KBi was
90 carried out with a NETZSCH Simultan STA 409 EP analyzer. DT-TG data were collected in
91 air using a $10^\circ\text{C}/\text{min}$ heating rate over the $20\text{-}1100^\circ\text{C}$ temperature range to determine the
92 amount of structural water, and temperatures characteristic of structural changes.

93 Total contents of Mn and interlayer K were determined using a Perkin-Elmer Optima
94 3000 ICP-AES after digestion of about 8 mg of birnessite powder in 200 mL of a 1% HNO_3 /
95 0.1% $\text{NH}_3\text{OH}\cdot\text{Cl}$ matrix. The mean oxidation degree of manganese in KBi was determined by
96 potentiometric titration using $(\text{NH}_4)_2\text{Fe}(\text{SO}_4)$ Mohr salt and sodium pyrophosphate.^{72,73} The
97 mean oxidation state, $2x$, in combination with the atomic ratio $y = \text{K}/\text{Mn}$ determined from the
98 chemical analyses, allows calculating the structural formula of KBi using the relation:⁷⁰



100 where $w = \frac{2x + y}{2}$, and \square represents vacant layer site. This structural formula can be refined
101 by taking into account the amounts of interlayer H₂O molecules deduced from the DT-TG
102 analysis.

103 **X-Ray Diffraction Data Collection.** Powder XRD patterns were recorded using a
104 Bruker D5000 powder diffractometer equipped with a Kevex Si(Li) solid detector and CuK α
105 radiation. Intensities were recorded from 5 to 80° 2 θ , using 0.04° 2 θ steps, and a 40 sec
106 counting time per step. A TTK450 Anton Paar chamber was used to record patterns from a
107 KBi sample heated *in situ*. The initial KBi sample before thermal treatment will be hereafter
108 referred to as sample RoomT-KBi, while 100-KBi, 150-KBi, 250-KBi and 350-KBi refer to
109 KBi samples heated *in situ* at 100°C, 150°C, 250°C and 350°C, respectively. KBi sample was
110 heated *in situ* to the desired temperature at a 6°C/min rate similar to that used for the DT-TG
111 analyses. A 2-hour plateau at fixed temperature was observed before starting XRD data
112 collection so that the sample may reach its thermal equilibrium. All KBi XRD patterns from
113 the temperature series were recorded successively in a single continuous experiment,
114 increasing the temperature stepwise. The AfterT-KBi sample will hereafter refer to the KBi
115 sample after the complete thermal treatment up to 350°C and subsequent cooling to room
116 temperature.

117 **Simulation of Powder XRD Patterns.** One of the effective ways to determine the actual
118 structure of defective layered compounds is the calculation of powder XRD patterns using the
119 mathematical formalism described by Drits et al.⁷⁴ This trial-and-error fitting procedure has
120 been successfully used to determine the crystal-chemical structure of different natural and
121 synthetic birnessites containing random stacking faults or consisting of the interstratification
122 of different layer types.^{8,21,70,75-79} Details on the program used to simulate XRD patterns and
123 on the fitting procedure are given by Plançon and Drits et al.^{75,80,81} Specifically, the coherent
124 scattering domains in the layer plane were assumed to have a disk-like shape whose radius

125 was adjusted. For each sample, the background was assumed to be linearly decreasing over
126 the angular range. No preferred orientation was considered in agreement with the peculiar
127 geometry of particles clusters revealed by SEM observations. The quality of fit was estimated
128 over the 34° - 74° 2θ $\text{CuK}\alpha$ range using the usual R_{wp} parameter.

129

130

Results

131

132 **Size and Shape of KBi Particles.** SEM observations of KBi samples show that these
133 samples consist of ball-like particles having a 2-5 μm diameter (Figures 1a and 1b) as
134 described earlier.⁵⁷ A closer look at these ball-like particles reveals that they actually consist
135 of an aggregate of individual plate-like crystals that are strongly held together and whose
136 maximum length and thickness are $\sim 1 \mu\text{m}$ and $\sim 20 \text{ nm}$, respectively (Figures 1b and 1c).
137 These crystal shape and dimensions are very similar to those usually reported for natural
138 birnessite crystals or for their synthetic analogues obtained according various protocols,
139 except for the high temperature decomposition of KMnO_4 which leads to crystals
140 micrometer-sized along all directions.⁷⁰ A layer ‘crust’ covering part of the ball-like
141 aggregates is sometime observed (Figure 1b). This peculiar morphology of the aggregates
142 likely prevents the preferential orientation commonly observed for other varieties of natural
143 or synthetic birnessites when prepared for powder XRD analysis.

144 **Loss of Weight During Heating.** Thermogravimetric (TG) analysis of KBi shows four
145 distinct losses of weight labeled a-d in Figure 2a. The two low-temperature losses at $\sim 90^{\circ}\text{C}$
146 and $\sim 140^{\circ}\text{C}$ (a and b) are commonly assumed to correspond to adsorbed and interlayer water
147 whereas the one occurring between 250°C and 400°C (c) likely corresponds to the loss of
148 oxygen atoms from the octahedral layer framework in relation with the partial reduction of
149 Mn^{4+} to Mn^{3+} .^{57,68} A similar reduction of Mn^{4+} to Mn^{3+} and loss of structural O anions has
150 been reported for pyrolusite (MnO_2) at ~ 350 - 400°C .⁸² Finally, the strong endothermic peak in

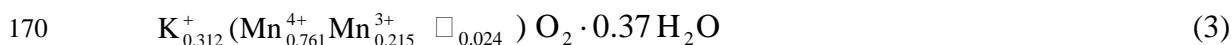
151 the DT curve and the associated weight loss at ~890°C (d) is most likely related to the
152 melting of KBi.

153 For sample AfterT-KBi losses of weight are observed at ~90°C, ~165°C, and ~910°C
154 (Figure 2b) which correspond to the endotherms a, b, and d, respectively, observed for
155 sample RoomT-KBi. However, in contrast with sample RoomT-KBi, sample AfterT-KBi
156 exhibits a weight gain at ~320°C, rather than a weight loss.

157 **Chemical Analyses and Structural Formula.** The K/Mn atomic ratio ($y = 0.320$) can
158 be calculated from ICP analytical results whereas the H₂O/Mn ratio (0.43) is deduced from
159 the 7.51% weight loss measured between 100°C and 220°C and corresponding to the loss of
160 structural water. Another 2.7% weight loss is observed over the 250-400°C range. Before the
161 thermal treatment, the structure of RoomT-KBi contains only Mn⁴⁺ cations as the measured
162 oxidation state of Mn is equal to 4.00 ± 0.02 , and its structural formula can thus be written as:



164 In contrast, the oxidation state measured for Mn in the AfterT-KBi sample is much lower
165 (3.78 ± 0.02), showing that AfterT-KBi sample contains ~22% of Mn³⁺ and ~78% of Mn⁴⁺
166 cations if the relative proportion of Mn²⁺ is assumed to be negligible. In addition, the 6.4%
167 weight loss measured between 100°C and 230°C after rehydration corresponds to the loss of
168 structural water. If the K/Mn ratio is unchanged after the rehydration of the heated KBi
169 sample at room temperature, the structural formula of AfterT-KBi can be written as:



171 **Indexing of the Experimental XRD Patterns.** Figure 3 compares the XRD patterns of
172 KBi recorded at room temperature (before and after thermal treatment) and at temperatures
173 ranging from 100-350°C. Following their indexing as described below, experimental and
174 calculated $d(hkl)$ values are listed in Table 2 for all KBi samples and the corresponding unit-
175 cell parameters are reported in Table 1. Note that Table 1 also contains the unit-cell
176 parameters of additional phases identified in samples 100-KBi, 350-KBi and AfterT-KBi

177 samples while fitting their respective XRD patterns with the trial-and-error approach
178 described by Drits et al.⁷⁴

179 *Sample RoomT-KBi.* The XRD pattern of RoomT-KBi can be indexed using a three-layer
180 rhombohedral ($3R$) unit cell having $a_{\text{rh}} = b_{\text{rh}} = 2.845 \text{ \AA}$, $\gamma = 120^\circ$ and $c = 21.492 \text{ \AA}$ (space
181 group $R\bar{3}m$) as described by Chen et al.⁵⁷ However, for later needs, the indexation was
182 performed systematically with an orthogonal base-centered unit cell having $a_{\text{ort}} = a_{\text{rh}}\sqrt{3} =$
183 4.923 \AA , $b_{\text{ort}} = b_{\text{rh}} = 2.845 \text{ \AA}$, $\gamma = 90^\circ$ and $c = 21.492 \text{ \AA}$ (Table 1). Going from low- to high-
184 angle values, the powder XRD pattern of RoomT-KBi (Figure 3a) contains a rational series
185 of basal reflections with a $d(003)$ value corresponding to a minimum periodicity of 7.164 \AA
186 along the \mathbf{c}^* axis followed by two families of $hk\ell$ reflections having for indices i) 20ℓ ($\ell = 3n$
187 $+ 1$, n integer) and 11ℓ ($\ell = 3n - 1$) over the 34° - 80° 2θ range, ii) 31ℓ and 02ℓ ($\ell = 3n$) over
188 the 64° - 80° 2θ range.

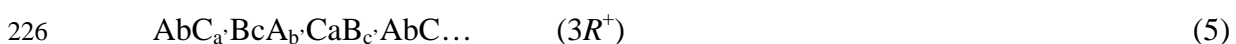
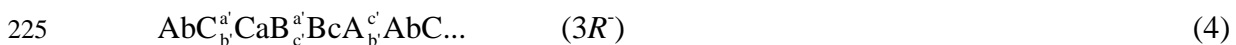
189 *Heated-KBi Samples.* XRD patterns obtained during heating of KBi sample are very
190 similar to that recorded on the initial RoomT-KBi sample and can also be indexed using $3R$
191 unit cells (unit-cell parameters being hereafter expressed in the orthogonal system). Figures
192 3b-d show that only intense dehydration occurs when heating the sample up to 250°C thus
193 inducing a significant decrease of the $d(003)$ value down to 6.46 - 6.42 \AA and related shifts of
194 non-basal reflections (Table 2). Figure 4 shows that the decrease of c parameter is
195 accompanied by a limited increase of a ($= b\sqrt{3}$) and b unit-cell parameters (Table 1), the
196 hexagonal layer symmetry being preserved up to that temperature ($a = b\sqrt{3}$, $\gamma = 90^\circ$). In
197 contrast, a dramatic increase of the lateral dimensions of the layer was observed ($b = 2.868 \text{ \AA}$
198 – Table 1 – Figure 4) when heating the sample to 350°C . A careful examination shows that
199 with increasing temperatures 00ℓ diffraction lines are broadened and that their asymmetry is
200 increased. For example, the tail which is present on the low-angle side of both 003 and 006
201 reflections above 100°C results in a shoulder at 350°C (inset on Figure 3e) thus suggesting

202 the presence of crystals with a larger dimension along the \mathbf{c}^* axis. When temperature is
 203 increased to 350°C, $hk\ell$ reflections are broadened in addition to 00ℓ ones, the profiles of
 204 some of these reflections becoming asymmetrical. In addition, for some of these $hk\ell$
 205 reflections the mismatch between measured and calculated $d(hk\ell)$ values exceeds the
 206 experimental error (Table 2). As discussed below, these specific features of experimental
 207 XRD profiles are related to the heterogeneous phase composition of sample 350-KBi.

208 *Sample AfterT-KBi.* Following the thermal treatment up to 350°C, the XRD pattern
 209 recorded at room temperature on sample AfterT-KBi is dramatically modified as compared to
 210 those of both RoomT-KBi and 350-KBi. The diffraction pattern can be indexed assuming a
 211 one-layer monoclinic unit cell ($1M$) with $a = 5.130 \text{ \AA}$, $b = 2.850 \text{ \AA}$, $c = 7.131 \text{ \AA}$, $\beta = 101.0^\circ$
 212 (space group $C2/m$). The octahedral layers of AfterT-KBi have thus an orthogonal symmetry
 213 with $a > b\sqrt{3}$ whereas all other samples had a hexagonal layer symmetry. Adjacent layers are
 214 shifted with respect to each other by $c \cdot \cos\beta = -0.260 a$ along the \mathbf{a} axis, and the basal spacing
 215 $d(001)$ is equal to $c \cdot \sin\beta = 7.000 \text{ \AA}$. As for sample 350-KBi, $hk\ell$ reflections of AfterT-KBi
 216 have broad and asymmetrical profiles and for some of them a noticeable discrepancy between
 217 $d_{\text{exp}}(hk\ell)$ and $d_{\text{cal}}(hk\ell)$ can be observed (Table 2). It will be shown below that these specific
 218 features of experimental XRD profiles are related to the heterogeneous phase composition of
 219 sample AfterT-KBi.

220 **Quantitative Structure Determination.**

221 *Layer Stacking Sequence of the 3R Samples.* In agreement with previous reports,⁵⁷
 222 RoomT-KBi sample was indexed with a three-layer rhombohedral ($3R$) unit cell in space
 223 group $R\bar{3}m$. However, two distinct structure models match these requirements. Using the
 224 close-packing formalism, these idealized models are described as:



227 where A, B and C represent the positions of layer oxygen atoms (O_{layer}), a, b and c the
228 positions of the layer Mn cations (Mn_{layer}) and a', b' and c' the positions of interlayer K
229 cations. In the first model ($3R^-$ polytype), adjacent layers are shifted with respect to each
230 other by $-a/3$ along the **a** axis, thus leading to the prismatic coordination of interlayer species.
231 In the second model ($3R^+$ polytype), adjacent layers are shifted with respect to each other by
232 $+a/3$ along the **a** axis, interlayer species being then octahedrally coordinated. For the two
233 polytypes, diffraction lines have identical positions but differ by their relative intensities. The
234 intensity of the 20ℓ ($\ell = 3n + 1$) reflections is indeed much lower than that of 11ℓ ($\ell = 3n - 1$)
235 reflections for the $3R^-$ polytype, whereas the 20ℓ reflections of the $3R^+$ polytype are more
236 intense than the 11ℓ ones (Figure 5a). The total intensity calculated for overlapped 31ℓ and
237 02ℓ ($\ell = 3n$) reflections are similar for the two stacking modes. From the comparison of their
238 experimental XRD patterns (Figure 3) with those calculated for the two polytypes, RoomT-
239 KBi and all heated samples clearly correspond to the $3R^-$ polytype, their layers being
240 systematically shifted with respect to each other by $-a/3$ along the **a** axis.

241 *Sample RoomT-KBi.* In the initial structure model, Mn_{layer} was located at the origin of the
242 unit cell, and O_{layer} had coordinates (0.333, 0, ± 0.046) to match the 2.00 Å layer thickness
243 previously reported for phyllophanates.^{70,75-79,83,84} In agreement with the proposed
244 structural formula (eq 2) it was initially assumed that 0.924 Mn cations are present per layer
245 octahedron. According to Chen et al.,⁵⁷ both interlayer K^+ cations and H_2O molecules are
246 located on the faces of the trigonal prisms formed by O_{layer} from adjacent layers (Figure 6 –
247 Position 1). For high-temperature K-birnessite with a similar layer octahedral composition,
248 Gaillot et al. proposed an alternative position in the center of the interlayer prismatic cavity
249 (Figure 6 – Position 2).⁷⁰ In this alternative position, K is located above (or below) the empty
250 tridentate cavity of the lower (or upper) layer and below (or above) a vacant or occupied Mn
251 octahedron of the upper (or lower) layer. The intensity distributions calculated for 20ℓ and

252 11ℓ reflections assuming either model are compared in Figure 7a to the experimental XRD
253 patterns of KBi samples. In both cases, calculated and experimental XRD patterns are similar
254 and the solution does not appear univocal. Contrastingly, the intensity distribution of 31ℓ and
255 02ℓ reflections is extremely sensitive to the atomic coordinates of interlayer species.
256 Specifically, after normalization of the calculated $310/020$ maximum to the experimental one,
257 the calculated $313/023$ reflection is significantly lower than the experimental one when K^+ is
258 located in the center of the trigonal prisms and higher when K^+ is located in the prism's faces
259 (Figure 7b). The intensity ratio between these two diffraction maxima can thus be used to
260 constrain the position of interlayer K^+ cations, and the XRD simulations has thus been
261 performed over the 34° - 74° 2θ range for all KBi samples to include 31ℓ and 02ℓ reflections
262 along with 20ℓ and 11ℓ ones. The best fit to the experimental XRD pattern (Figure 7b) was
263 obtained when within each interlayer prism the site of K^+ is split, K^+ being shifted from the
264 center of the prism towards its faces [Figure 6 – Position 3; (-0.24, 0, 0.167)]. A similar
265 position for interlayer K^+ cations site was refined for high-temperature KBi samples with a
266 similar layer octahedral composition.⁷⁰ In the optimum structure model for sample RoomT-
267 KBi, H_2O molecules were located in the center of the interlayer space shifted from the edges
268 of the trigonal prisms towards their centers, in six positions equivalent to (0.5, 0, 0.167)
269 (Position 4 – Figure 6). The inter-atomic distance between these H_2O molecules and the
270 nearest O_{layer} from adjacent layers ($O_{\text{layer}}-H_2O = 2.707 \text{ \AA}$ with a $O_{\text{layer}}-H_2O-O_{\text{layer}}$ angle equal
271 to 144.7°) allows the formation of strong H-bonds which contribute significantly to the
272 cohesion between layers.

273 However, when only the above phase is considered, a significant misfit to the
274 experimental XRD pattern is visible at the tails of each diffraction maximum (Figure 5b –
275 $R_{\text{wp}} = 15.77\%$). This misfit was assumed to result from the presence in sample RoomT-KBi
276 of an additional fine-grained phase whose structure is identical to that of the main phase but
277 exhibiting a high structural disorder. The contribution of this very disordered phase (Figure

278 5c) has been included in all simulations to improve fit quality. This phase possibly
279 corresponds to the material holding KBi crystals together and sometimes forming a “crust”
280 over the ball-like aggregates (Figure 1b). Accordingly, the best fit to the RoomT-KBi
281 experimental data (Figure 5d – $R_{wp} = 8.90\%$) was obtained for a physical mixture (70:30
282 ratio) of a well-crystallized $3R$ phase containing 5% of random stacking faults (W_R) and of a
283 quasi-turbostratic phase ($W_R \sim 75\%$) having a smaller coherent scattering domain size
284 (CSDS) in the **ab** plane (70 Å vs 300 Å). In the quasi-turbostratic phase, adjacent layers with
285 a well-defined stacking mode are shifted with respect to each other by $-a/3$ along the **a** axis.
286 Although present in small proportion in the main $3R$ phase ($W_R = 5\%$), random stacking
287 faults significantly increase the width of $20\ell/11\ell$ reflections with increasing ℓ index (data not
288 shown). This peak broadening, together with the presence of the poorly crystalline phase,
289 impaired the use of conventional structure refinement techniques, including the Rietveld
290 technique. As a consequence the structural characterization of KBi samples was performed
291 with the trial-and-error method described by Drits et al.⁷⁴ Atomic coordinates, site
292 occupancies and other structural parameters used to obtain the best possible agreement
293 between experimental and calculated XRD patterns are listed in Table 3 whereas selected
294 inter-atomic distances are reported in Table 4.

295 *Sample 100-KBi.* The main structural features of 100-KBi XRD pattern are essentially
296 unchanged, as compared to that of RoomT-KBi. Interlayer water was assumed to be present
297 in most interlayers, in agreement with the DT-TG data which indicates that only adsorbed
298 H₂O molecules were lost at 100°C (first endothermic DT peak at ~90°C) and with the limited
299 decrease of the unit-cell *c* parameter. The structure model determined for sample RoomT-
300 KBi was thus used as a starting point for calculation of XRD patterns, after adjusting unit-cell
301 parameters to match the experimentally determined peak positions. The *x* coordinate of
302 interlayer H₂O molecules was changed (from 0.500 to 0.450 – Table 3) to better match the
303 experimental distribution of intensity (Figure 8a – $R_{wp} = 18.59\%$). In addition, the degree of

304 structural ordering and the crystallinity of KBi was found to be lower at 100°C than at room
305 temperature. The proportion of random stacking faults was indeed increased from 5 to 12% in
306 the ordered structure, whereas its CSDS in the **ab** plane was decreased from 300 to 230 Å.
307 The shoulder on the high-angle side of the 115 maximum which is visible on 100-KBi
308 experimental pattern (arrow – Figure 8a) was reproduced assuming the presence of a mixed-
309 layer structure (MLS – Figure 8b). In this MLS, 30% of the layers are identical to the ones in
310 the main ordered phase. The remaining 70% have the same layer structure but no interlayer
311 water, and thus exhibit a lower unit-cell *c* parameter (Table 1 – Figure 8b). Other structural
312 parameters such as unit-cell *b* parameter, cation occupancy of the Mn_{layer} site, and position of
313 interlayer K⁺ were identical to those determined for sample RoomT-KBi (Table 3). The
314 partial dehydration observed in the accessory MLS is in agreement with the DT-TG results,
315 and with the tailing of the 006 reflection towards high angles. The best fit to the experimental
316 data (Figure 8c – $R_{wp} = 12.24\%$) was obtained for a physical mixture of 77% of a fully
317 hydrated periodic $3R$ polytype, 8% of the accessory and partially dehydrated MLS, and 15%
318 of a poorly crystalline phase exhibiting a quasi-turbostratic stacking ($W_R \sim 75\%$) and a small
319 CSDS in the **ab** plane (70 Å). Structural parameters characterizing the optimal model for
320 hydrated layers and selected inter-atomic distances are listed in Tables 3 and 4, respectively.
321 Parameters of the dehydrated layers are similar to those determined for sample 150-KBi and
322 reported in Table 3.

323 *Sample 150-KBi.* DT-TG results show that at 150°C KBi dehydration is complete as the
324 endotherm maximum was obtained at ~140°C. Accordingly, the XRD pattern reveals a much
325 smaller periodicity along the **c*** direction ($d(003) = 6.494$ Å) leading to a strong decrease of
326 the unit-cell *c* parameter. Simultaneously, the unit-cell *b* parameter is slightly enlarged most
327 likely as the result of an increased thermal motion and/or to better accommodate the presence
328 of K⁺ cations in dehydrated interlayers. Apart from the shift of diffraction lines due to the
329 collapse of KBi layers, the experimental XRD pattern of sample 150-KBi looks essentially

330 similar to those obtained at lower temperatures indicating that the structure of KBi is
331 essentially unaffected by the dehydration. Consistently, in the optimum structure model K^+
332 cations were located at the interlayer mid-plane, and shifted towards the faces of the
333 prismatic cavities in 6 positions equivalent to $(-0.27, 0, 0.167)$, although H_2O molecules were
334 no longer present in the interlayer space. Note that this structure model is very similar to that
335 determined for the dehydrated layers present in sample 100-KBi. The two models differ from
336 each other only by the lateral unit-cell dimensions and interlayer K^+ cations positions (Tables
337 1 and 3). The best fit to the experimental data (Figure 8d – $R_{wp} = 8.92\%$) was obtained for a
338 physical mixture of 61% of a well-crystallized phase ($W_R = 10\%$, CSDS in the **ab** plane =
339 230 \AA) and 39% of a quasi-turbostratic phase ($W_R \sim 75\%$, CSDS = 70 \AA). Structural
340 parameters characterizing the optimal model and selected inter-atomic distances are listed in
341 Tables 3 and 4, respectively.

342 *Sample 250-KBi Model.* The structure model determined for sample 250-KBi is also
343 similar to the ones described above, although both the degree of structural ordering and the
344 crystallinity keep degrading. The main ordered phase contains indeed 17% of random
345 stacking faults, its average CSDS in the **ab** plane being 180 \AA . The relative proportion of the
346 quasi-turbostratic phase providing the best fit to the experimental data (Figure 8e – $R_{wp} =$
347 9.97%) is 25%. Structural parameters characterizing the optimal model and selected inter-
348 atomic distances are listed in Tables 3 and 4, respectively.

349 *Sample 350-KBi.* The structure can be described to a large extent as a $3R^-$ polytype, but
350 significant structural changes are visible on the XRD pattern of 350-KBi (Figure 3e). In
351 particular, the shoulder on the low-angle side of the 006 maximum (inset on Figure 3e)
352 suggests the presence of layers with an interlayer spacing larger than that of the main phase.
353 In addition, there is a strong increase of the unit-cell b parameter from $2.845\text{-}2.851 \text{ \AA}$ (25-
354 250°C) to 2.868 \AA at 350°C (Table 1, Figure 4) although layer symmetry remains hexagonal.
355 This abrupt and dramatic increase cannot result solely from thermal motion as the unit-cell

dilatation usually depends linearly on the temperature if the structure or the electronic state (for redox sensitive elements) is not modified. Rather, it is likely that at this temperature Mn^{4+} was partially reduced to Mn^{3+} . As a result, $\langle \text{Mn-O} \rangle$ distance was increased and lateral dimensions of the unit cell were enlarged to accommodate this augmentation. $\langle \text{Mn-O} \rangle$ increases indeed from 1.912 Å for Mn^{4+} (determined for $\lambda\text{-MnO}_2$)⁸⁵ to 2.04 Å for Mn^{3+} in crednerite and other Mn-oxyhydroxides.^{86-88,89, Norrestam, 1967 #789} As a consequence of the presence of trivalent Mn_{layer} , the layer charge deficit was assumed to derive essentially from the coexistence of heterovalent Mn_{layer} cations within the octahedral layer and no Mn vacant sites were considered in the structure model of 350-KBi (see structural formula – eq 3). Apart from the occupancy of the Mn_{layer} site, atomic coordinates and occupancies of the various sites were considered to be identical to those determined for sample 250-KBi. The resulting $3R^-$ structure allowed reproducing the main features of the experimental diffraction pattern, except for the strong shoulder on the low-angle side of the 115 reflection which is visible only for sample 350-KBi (arrow on Figure 9a). The position of this shoulder is close to that of the 204 reflection of $3R^-$ varieties, this reflection being extremely weak for the $3R^-$ polytype but strong for the $3R^+$ polytype (Figure 5a). Layers stacked with a $+a/3$ interlayer displacement along the **a** axis (polytype $3R^+$) are thus likely present in sample 350-KBi. Since the 204 maximum appears as a broad shoulder tailing towards the 115 reflection of the $3R^-$ polytype, it is likely that $3R^+$ and $3R^-$ structural fragments coexist within the same crystals. The diffraction effects resulting from the interstratification of $3R^+$ and $3R^-$ structural fragments within the same crystallites may be predicted from the considerations developed by Drits and coworkers.^{75,90,91} By applying Méring's approach, which was developed initially for $00l$ reflections, to hkl reflections Drits and coworkers were able to demonstrate that the diffraction maxima observed for the MLS resulting from the random interstratification of fragments of periodic structures having similar layer structure but different interlayer displacements are located between the maxima corresponding to the individual periodic

382 structures. The actual position and intensity of these reflections depend on the proportion of
383 each type of the interstratified fragments.⁹⁰⁻⁹² As for clay minerals,⁹⁰ this type of structural
384 defect is common in birnessite.^{70,76,78,79} In agreement with the above considerations, the 204
385 shoulder at $\sim 41.5^\circ 2\theta$ in the 350-KBi XRD pattern was thus reproduced (Figure 9b) with the
386 contribution of a MLS containing 30% of layers shifted by $-a/3$ along the **a** axis (A layers,
387 corresponding to fragments of a $3R^-$ polytype) and 70% of layers shifted by $+a/3$ along the **a**
388 axis (B layers, corresponding to fragments of a $3R^+$ polytype). The two layer types were
389 randomly interstratified, and they both had unit-cell parameters $a = 4.997 \text{ \AA}$, and $b = 2.885 \text{ \AA}$.
390 The interlayer configuration within B fragments ($3R^+$ polytype) is different from that in the A
391 fragments because of the different layer stacking mode. In the former fragments, interlayer
392 K^+ cations have an octahedral rather than prismatic coordination and were found to be located
393 in position $(-0.3, 0, 0.167)$ – Figure 10). With respect to a given layer, this position of
394 interlayer K^+ , above and below the empty tridentate cavity of adjacent octahedral layers, is
395 similar to that in the A layers.

396 The best fit to the experimental XRD pattern (Figure 9c – $R_{wp} = 9.92\%$) was obtained for
397 a physical mixture of quasi-periodic $3R^-$ crystals (95:5 ratio between A and B layers,
398 respectively – $W_R = 10\%$), a $3R^-/3R^+$ MLS (30:70 ratio between A and B layers, respectively
399 – $W_R = 30\%$), and a quasi-turbostratic structure ($W_R = 75\%$ – $3R^-$ ordered layer stacking) in a
400 40:20:40 ratio. The CSDS in the **ab** plane is slightly larger for 350-KBi crystals as compared
401 to 250-KBi crystals (230 \AA and 200 \AA for the quasi-periodic $3R^-$ structure and the MLS,
402 respectively, as compared to 180 \AA).

403 *Sample AfterT-KBi.* XRD patterns of KBi recorded at room temperature before and after
404 the thermal treatment differ strikingly (Figures 3a and 3f). Specifically, whereas the RoomT-
405 KBi sample was dominated by a $3R^-$ periodic structure, simulation of its XRD patterns
406 showed that sample AfterT-KBi consisted of two phases present in equal proportions. In one
407 of the phases 90% of the layers are stacked according to a monoclinic $1M$ structure. These

408 layers are interstratified with layers forming $3R^-$ structural fragments (Figure 11a – $R_{wp} =$
 409 23.03%). The layers forming the $1M$ and $3R^-$ subsequences are partially incommensurate. $1M$
 410 layers exhibit an orthogonal layer symmetry with unit-cell parameters $a_{ort} = 5.130 \text{ \AA}$, $b_{ort} =$
 411 2.850 \AA ($a_{ort} > b_{ort}\sqrt{3}$), $c = 7.131 \text{ \AA}$, $\beta = 101.0^\circ$, $T_x = c \cdot \cos\beta = -0.260 a$. Unit-cell parameters
 412 of the $3R^-$ fragments present in sample AfterT-KBi ($a_{ort} = b_{ort}\sqrt{3} = 4.971 \text{ \AA}$, $b_{ort} = 2.870 \text{ \AA}$, $c =$
 413 21.150 \AA) are considerably increased as compared to those reported for RoomT-KBi ($a_{ort} =$
 414 4.923 \AA , $b_{ort} = 2.845 \text{ \AA}$, $c = 21.492 \text{ \AA}$ – Table 1, Figure 4). This increase is consistent with
 415 the structural formula proposed for this sample (eq 3) which indicates the presence of a
 416 significant proportion of Mn^{3+} cations in vacancy-free layers. As indicated by their
 417 orthogonal layer symmetry, $1M$ layers also contain a significant proportion of Mn^{3+} cations in
 418 vacancy-free layers. In these latter layers, interlayer K^+ cations and H_2O molecules are
 419 located in $(-0.40, 0, 0.5)$ and $(-0.45, 0, 0.5)$, respectively (Figure 12 – Tables 4, 5). These
 420 positions are similar to the main undifferentiated (K, H_2O) position found by Post and Veblen
 421 $(-0.413, 0, 0.5)$,⁸³ provided that their x position is given in projection normal to the **ab** plane.
 422 As both types of interstratified layer fragments consist of vacancy-free layers and likely
 423 contain a similar proportion of Mn^{3+} , the origin of their incommensurability is to be sought in
 424 the orientation distribution of distorted Mn^{3+} layer octahedra (see Discussion). As a result of
 425 the thermal treatment and of the induced chemical and structural modifications, the $1M/3R^-$
 426 MLS contains a high proportion of random stacking faults ($W_R = 25\%$) as compared to low-
 427 to-medium temperature KBi samples ($W_R = 5\text{-}17\%$ for RoomT-, 100-, 150-, and 250-KBi
 428 samples).

429 The second phase present in sample AfterT-KBi was poorly crystallized (CSDS in the **ab**
 430 plane = 70 \AA) and possessed a quasi-turbostratic structure ($W_R = 75\%$). $3R^-$ and $1M$ structural
 431 fragments coexist in a 4:1 ratio among layers having a well-defined stacking (random
 432 interstratification – Figure 11b). Both $3R^-$ and $1M$ layers are identical in the two phases (unit-
 433 cell parameters, coordinates and occupancies of the different sites – Table 4), and it was

434 assumed that randomly stacked layers had the same lateral dimensions as $3R^-$ layers. The best
435 fit to the experimental XRD pattern is shown in Figure 11c ($R_{wp} = 8.67\%$). Structural
436 parameters characterizing the optimal model for both $3R^-$ and $1M$ fragments and selected
437 inter-atomic distances are listed in Tables 3 and 4, respectively.

438

439

Discussion

440

441 The determination of structure models for all KBi samples allowed complementing our
442 knowledge of crystal chemistry and structure of KBi obtained from the decomposition of
443 KMnO_4 under mild hydrothermal conditions and of their modifications upon temperature
444 increase. In the following, the origin of the layer charge will be determined in the original
445 sample and as a function of temperature along with structural changes. In particular the
446 partial reduction of Mn_{layer} and the migration of vacant sites within layer, which is associated
447 to the departure of O_{layer} , will be discussed. Finally, the location of interlayer species will be
448 analyzed as a function of temperature from its influence of layer structure stability.

449 Crystal-Chemistry of Sample RoomT-KBi

450 *Cation Composition and Layer Structure.* Titration of Mn oxidation degree shows that
451 the Mn oxidation state is reduced from +VII to +IV when KBi is obtained from the
452 hydrothermal decomposition of KMnO_4 and that no Mn^{3+} is formed. To our present
453 knowledge, this protocol is actually the only abiotic one that allows obtaining synthetic
454 birnessite crystals exhibiting a three-dimensional ordering and containing only Mn^{4+} cations,
455 which seems to be an important feature for electrochemical applications.⁶⁹ From the
456 reduction of KMnO_4 by MnCl_2 in near neutral conditions Villalobos et al. also synthesized a
457 birnessite sample ($\delta\text{-MnO}_2$) containing only Mn^{4+} cations in the octahedral layers, but this
458 birnessite was totally turbostratic ($W_R = 100\%$) and presented extremely limited development
459 of the layers in the **ab** plane.⁹³

460 In agreement with the sole presence of Mn^{4+} cations within octahedral layers, individual
461 and average Mn-O distances are equal to 1.92 Å (± 0.01) in RoomT-KBi. This value is indeed
462 typical for MnO_2 compounds.⁸⁷ For example, similar $\langle \text{Mn-O} \rangle$ distances were reported in the
463 Mn^{3+} -free layers of chalcophanite (1.923 Å) and of λ - MnO_2 (1.912 Å).^{85,94} As a consequence,
464 KBi layers likely contain ~7% of vacant octahedra which represent the sole source of layer
465 charge deficit, in agreement with the proposed structural formula (eq 2). The layer cation
466 composition and the source of layer charge deficit in hydrothermal KBi are thus similar to
467 those observed for the sample KBi_8 obtained from the thermal decomposition of KMnO_4 at
468 800°C whose Mn^{3+} -free layers contain 12% of vacant octahedra.⁷⁰ As in other
469 phyllomanganates, octahedra building up KBi layers are flattened along the c^* axis as a result
470 of the electrostatic repulsion between adjacent Mn_{layer} . The length of shared O-O edges in
471 RoomT-KBi crystals (2.59 Å) is thus shorter than that of O-O edges on the basal surfaces of
472 the crystals (2.84 Å - Table 4).

473 *Interlayer Structure.* Interlayer K^+ cations occupy one of the six positions equivalent to
474 the (-0.24, 0, 0.167) site (Position 3 – Figure 6a). Each site in the interlayer mid plane is
475 shifted from one face of the prism towards its center. Interlayer K^+ cations are coordinated by
476 four O_{layer} atoms at ~2.970 Å. Two H_2O molecules at 2.924 Å and 3.222 Å complete their
477 first coordination shell. These short K- O_{layer} bond lengths significantly contribute to the
478 cohesion between adjacent layers, together with short H_2O - O_{layer} distances (2.705 Å) which
479 allow for strong H-bonds. The shift of interlayer K^+ cations from the center of the prism
480 decreases unfavorable electrostatic repulsion with the nearest Mn_{layer} . The position
481 determined for interlayer K^+ cations in RoomT-KBi is similar to that refined on a KBi_8
482 monocrystal in which average K-O distances were also compatible with a 6-fold coordination
483 (4 O_{layer} and 2 H_2O).⁷⁰

484 In contrast to sample KBi_8 , interlayers of RoomT-KBi are devoid of Mn^{3+} cations and
485 the layer charge deficit is compensated for by the sole presence of 0.30 interlayer K^+ cations.

486 To provide local charge compensation, these cations should be close to the source of layer
487 deficit of charge. Specifically, O_{layer} coordinated to 2 Mn_{layer} and a vacant layer site are
488 strongly undersaturated, ideally receiving only $2 \times 0.667 = 1.333$ vu (valence unit).
489 Therefore, the location and distribution of K^+ cations is most likely related to the distribution
490 of vacant sites so as to provide local charge compensation. The absence of super-reflections
491 in both XRD and selected-area electron diffraction patterns (data not shown) suggest that
492 vacant sites and associated interlayer K^+ cations are randomly distributed in KBi.

493 **Crystal Chemistry of KBi from 100-250°C**

494 DT-TG results show, in agreement with XRD, that dehydration of KBi layers initiates at
495 $\sim 90^\circ\text{C}$ and is complete at $\sim 150^\circ\text{C}$. Apart from the departure of the interlayer H_2O molecules,
496 which leads to the collapse of KBi layers, heating of KBi up to 250°C does not alter its basic
497 structure, which can be indexed in the $R\bar{3}m$ space group ($3R$ polytype) over this temperature
498 range. The hexagonal symmetry of KBi layers is thus preserved and only a minor increase of
499 unit-cell dimensions is observed, most likely as a result of thermal motion (Table 1 – Figure
500 4). Once H_2O molecules have left the structure, the six-fold coordination of K^+ is likely
501 ensured by the nearest six O_{layer} defining the interlayer prismatic cavity. As a result of the
502 dehydration, interlayer K^+ cations thus slightly migrate from $(-0.24, 0, 0.167)$ at room
503 temperature towards the center of the prism at 250°C $[(-0.29, 0, 0.167) - \text{Table 3}]$ most likely
504 to provide more appropriate $\text{K}-O_{\text{layer}}$ distances after the partial layer collapse. In addition, the
505 relative proportion of random stacking faults (W_R) steadily increases (from 5-17%) with
506 increasing temperature in the well-crystallized phases, whereas the CSDS in the **ab** plane is
507 decreasing from 300 \AA to 180 \AA . In contrast, the CSDS along the **c*** axis in the well-
508 crystallized phases remains unchanged with temperature (6 layers in average) and the relative
509 proportion of the fine-grained quasi-turbostratic phase does not vary significantly with
510 temperature (Table 3).

511 **Structure Modification of KBi at 350°C**

512 Whereas KBi structure is stable up to 250°C, significant chemical and structural
513 modifications occur when temperature reaches 350°C. Specifically, modifications affecting
514 unit-cell dimensions, Mn oxidation state and related weight loss reported in results section
515 will be discussed below.

516 *Evolution of Layer Dimensions and Mn Oxidation State.* The temperature increase from
517 250°C to 350°C does not modify the layer symmetry. However, a significant increase of the
518 layer unit-cell parameters is observed from $b = 2.851 \text{ \AA}$ at 250°C to $b = 2.868 \text{ \AA}$ and 2.885 \AA
519 for the layers of the $3R'$ phase and of the MLS, respectively. A significant weight loss
520 (2.7 wt% – Figure 2) also accompanies the temperature increase. As mentioned above, such
521 dramatic increase of the unit-cell dimensions within the **ab** plane is likely not related to
522 thermal motion but rather to the partial reduction of Mn^{4+} to Mn^{3+} . Chemical analysis of KBi
523 crystals after cooling indeed revealed a much lower Mn mean oxidation state (3.78 for
524 sample AfterT-KBi vs 4.00 for sample RoomT-KBi). Partial reduction from Mn^{4+} to Mn^{3+}
525 most likely account for the observed decrease which is likely due to the presence of 22% of
526 Mn^{3+} cations in the heated sample. Herbstein et al. also observed a weight loss (3.7 wt%)
527 when heating a $\text{K}_{0.5}\text{Mn}_{0.875}\text{O}_2$ sample to ~500°C and associated this effect with an oxygen
528 loss, which was in turn hypothesized to result from the partial reduction of Mn^{4+} to Mn^{3+} .^{57,68}
529 Because $\langle \text{Mn-O} \rangle$ distances are longer for Mn^{3+} (2.04 Å) than for Mn^{4+} cations (1.912 Å), the
530 presence of such a high amount of Mn^{3+} in KBi layers is responsible for the significant
531 increase of the unit-cell dimensions within the **ab** plane.

532 The hexagonal layer symmetry may at first sight seem to contradict the presence of Mn^{3+}
533 cations in the layer. Mn^{3+} cations are known to be affected by the Jahn-Teller effect that
534 lowers the symmetry of the 3d electron orbitals and distorts the octahedra leading to 4 short
535 and 2 long Mn-O distances. To minimize the resulting steric strains in Mn^{3+} -rich birnessites,
536 Mn^{3+} -octahedra distorted by the Jahn-Teller effect are commonly segregated in Mn^{3+} -rich
537 rows parallel to the **b** axis and are systematically oriented with their long Mn-O bonds (2.26Å

538 in crednerite)⁸⁶ along the **a** axis giving rise to an orthogonal layer symmetry. This cooperative
539 Jahn-Teller effect was reported for Na- and Ca-birnessite varieties obtained from the
540 oxidation of Mn²⁺,^{75,77,95} and for a K-birnessite variety obtained from reduction of Mn⁷⁺ at
541 1000°C.⁸⁴ In absence of cooperative Jahn-Teller effect the long Mn-O bonds of Mn³⁺
542 octahedra are randomly oriented at $\pm n120^\circ$ (n integer) with respect to the **a** axis. In this case,
543 the hexagonal symmetry of the layers is preserved, but the resulting increase of the average
544 octahedron size increases the unit-cell b parameter as compared to phylломanganate varieties
545 that are devoid of Mn³⁺ cations. Such a hexagonal layer symmetry with large unit-cell b
546 parameter (2.925 Å) have been reported for lithiophorite whose layers contain 33% of Mn³⁺
547 octahedra.⁹⁴

548 For sample 350-KBi, the unfavorable presence of strains in the layers is likely
549 compensated for by the thermal energy available at 350°C. The proposed model is supported
550 by the experimental results obtained by Gaillot et al. for a KBi sample obtained from the
551 thermal decomposition of KMnO₄ at 1000°C (KBi₁₀₀).⁸⁴ This sample has a
552 Mn_{0.737}⁴⁺Mn_{0.246}³⁺□_{0.017} layer cation composition, orthogonal layer symmetry with $a = 5.155$ Å,
553 $b = 2.846$ Å, $a/b = 1.811$, and exhibits an ordered distribution of Mn³⁺- and Mn⁴⁺-octahedra
554 in its layers. The layer symmetry of KBi₁₀₀ sample becomes hexagonal with an increase of
555 the unit-cell b parameter to 2.895 Å when heated *in situ* to 350°C, in relation with the
556 redistribution of distorted Mn³⁺-octahedra orientations at $\pm n120^\circ$ (n integer) with respect to
557 the **a** axis with equal probability for all three possible values of n . The abrupt increase of the
558 unit-cell parameter b for sample 350-KBi can thus be considered as additional evidence for
559 the presence of a significant amount of Mn³⁺ octahedra in 350-KBi layers, and for the partial
560 reduction of Mn⁴⁺ to Mn³⁺ at 350°C.

561 *Loss of Weight and Associated Structural Transformation of the Layer (Loss of O_{layer} and*
562 *Migration of Vacant Layer Sites).* Together with the formation of layer Mn³⁺ cations and with
563 the associated increase of the unit-cell a and b parameters, the temperature increase up to

564 350°C induces a 2.7% weight loss over the 250-400°C range. This weight loss likely results
 565 from the migration of vacant layer octahedra and from the induced formation of vacancy-free
 566 layers. A significant temperature increase can indeed allow the migration of Mn_{layer} to the
 567 nearest vacant sites forming new vacant sites. Consistently, sample AfterT-KBi, whose layers
 568 are essentially devoid of vacant sites, exhibits a weight gain rather than a weight loss over the
 569 250-400°C range (Figure 2b). Similar process of cation migration within octahedral layers
 570 has been described for example in 2:1 phyllosilicates. During the dehydroxylation of Fe³⁺-
 571 and Mg²⁺-rich dioctahedral micas, which occurs at ~450-600°C, octahedral Fe³⁺ and Mg²⁺
 572 cations migrate within the layer to the adjacent vacant octahedron to restore the structure
 573 stability which was disturbed following dehydroxylation.^{96,97,98} Cation migration has also
 574 been described when octahedral Fe³⁺ is reduced in 2:1 phyllosilicates.²⁴ In KBi layers, cation
 575 migration may result either in the migration of vacant sites to crystal edges or in the
 576 formation of vacancy clusters. In both cases, migration of vacant layer sites results in the
 577 reduction of the amount of vacant layer sites and in the loss of O_{layer}.

578 Loss of O_{layer} was shown to occur during the thermal reduction of synthetic pyrolusite
 579 (MnO₂) *in situ* between 300°C and 500°C.⁸² Using Electron Energy Loss Spectroscopy
 580 analysis, these authors were able to follow the reduction of Mn as a function of temperature
 581 by simultaneously determining the valence state of Mn and quantifying the relative
 582 proportion of oxygen vacancies created. In their study, Wang et al. found that reduction of
 583 MnO₂ occurs between 300-400°C with no visible structural change. However, they identified
 584 a “valence state conversion from 4+ to mixed valence state Mn⁴⁺, Mn³⁺ and Mn²⁺” associated
 585 with a decrease of the O/Mn ratio from 2.00 to ~1.64 (values taken from Figure 4 in Wang et
 586 al.).⁸² For our KBi sample, the extent of O_{layer} loss can be estimated theoretically from the
 587 modification of KBi structural formula induced by the heating. Transformation from sample
 588 Room-KBi (structural formula $K_{0.30}^{+} (Mn_{0.925}^{4+} \square_{0.075})O_2$ – eq 2) to sample 350-KBi leads to a
 589 $K_{0.30}^{+} (Mn_{0.625}^{4+} Mn_{0.300}^{3+})O_{1.85}$ structural formula for the latter vacancy-free layers. As a result the

590 theoretical weight loss associated to the departure of O_{layer} is ~ 2.5 wt%, in agreement with
591 that experimentally determined (2.7 wt%). The structural formula proposed for the vacancy-
592 free layers of sample 350-KBi can thus be transformed to $K_{0.324}^{+}(\text{Mn}_{0.676}^{4+}\text{Mn}_{0.324}^{3+})\text{O}_2$. A
593 similar agreement between calculated (4.0%) and experimentally determined (3.7%) weight
594 loss corresponding to the departure of O_{layer} is obtained for the sample studied by Herbstein et
595 al. using the structural formulae reported for their initial ($K_{0.50}^{+}(\text{Mn}_{0.875}^{4+}\square_{0.125})\text{O}_2$) and heat-
596 treated ($K_{0.50}^{+}(\text{Mn}_{0.375}^{4+}\text{Mn}_{0.50}^{3+})\text{O}_{1.75}$) specimens.⁶⁸

597 In conclusion, the weight loss observed over the 250-400°C temperature range for
598 synthetic birnessites may be considered as an evidence for the presence of vacant layer sites
599 in the sample at room temperature. In the present case, the weight loss results from the
600 thermally induced migration of the vacant sites from the structure to the edges of the layers,
601 thus inducing their vanishing and the associated loss of O_{layer} . Note that over the same
602 temperature range weight loss can be alternatively related to the dehydroxylation of
603 birnessite, as described for high-temperature KBi obtained at 800°C. {Gaillot, 2003 #2889}.
604 In this case, the weight loss results from the departure of OH groups initially bond to pre-
605 existing Mn^{3+} cations located in the interlayer region, above or below the layer vacant sites,
606 rather than in the octahedral layer.

607 *Layer Stacking Mode and Interlayer Structure.* In addition to the above structural
608 modifications, heating of KBi sample from 250°C to 350°C is accompanied by a strong
609 decrease of structural order and by a modification of the layer stacking for part of the layers.
610 Simulation of 350-KBi XRD pattern shows indeed that the main well-crystallized phase
611 keeps the initial $3R^{-}$ stacking sequence in which adjacent layers are shifted with respect to
612 each other by $-a/3$ along the **a** axis. In contrast, in the accessory MLS phase 70% of the
613 layers (B layers) are shifted by $+a/3$ along the **a** axis ($3R^{+}$ stacking sequence). These layers
614 are randomly interstratified with layers that kept their initial $3R^{-}$ polytype (A layers). This
615 layer stacking modification is likely related to the increased amount of Mn^{3+} in the octahedral

616 layers and to the associated decreased amount of vacant layer sites. At room temperature, half
617 of interlayer K^+ cations are most likely located above the empty layer tridentate cavity of the
618 lower layer and below a layer vacant octahedral of the upper one (or *vice versa*, $AbC_b^aCaB...$
619 stacking sequence – Figure 6). At 350°C, the proportion of vacant layer sites is strongly
620 decreased and in A layers interlayer K^+ cations are systematically facing an occupied Mn
621 octahedron on one side of the interlayer. The resulting K-Mn repulsion could destabilize the
622 layer stacking. By contrast, the initial prismatic coordination of interlayer K^+ observed in A
623 layers is modified in B layers to become octahedral ($AbC_{b'A}^{A'c'}BcA...$ – Figure 10). The
624 latter coordination seems more favorable as interlayer K^+ cations are located above and
625 below empty tridentate cavities of the two adjacent layers, the K-Mn repulsion being then
626 screened by O_{layer} . This interlayer configuration would allow a higher content of layer Mn^{3+}
627 and a lower vacant site content in layers of $3R^+$ fragments, and would explain the larger unit-
628 cell parameters of the layers in the accessory MLS as compared to those of layers making up
629 the $3R^-$ main phase ($b = 2.885 \text{ \AA}$ and 2.868 \AA , respectively)

630 *Degree of Crystallinity and Structural Order of 350-KBi.* The CSDS within the **ab** plane
631 of both the main $3R^-$ phase and of the MLS are slightly increased as compared to that of the
632 main 250-KBi phase (200-230 \AA vs 180 \AA , respectively – Table 3). This difference is likely
633 due to the dramatic rearrangement of layer cations resulting from the partial reduction of
634 Mn^{4+} to Mn^{3+} and from the subsequent migration of vacant layer octahedra. On the other
635 hand, the proportion of random stacking faults is very high in the main well-crystallized $3R^-$
636 phase ($W_R = 30\%$), most likely as the result of the unfavorable direct repulsion between
637 interlayer K^+ cations and Mn_{layer} ones induced by the evolution of KBi crystal-chemistry
638 occurring at this temperature.

639 **Structural Transformation of 350-KBi into AfterT-KBi.** Comparison of the phase
640 composition and structure in 350-KBi and AfterT-KBi samples allows proposing a structural
641 mechanism for the phase transformation occurring when sample 350-KBi is cooled down to

642 obtain sample AfterT-KBi. Indeed, the relative proportion of the main well-crystallized $3R^-$
643 phase in sample 350-KBi (40%) is similar to that of the proportion of the $1M/3R^-$ MLS in
644 sample AfterT-KBi (50%). To ease the following discussion, dehydrated $3R^-$ polytype in
645 sample 350-KBi and hydrated $3R^-$ polytype in sample AfterT-KBi will be hereafter referred
646 to as $3R^-_d$ and $3R^-_h$, respectively. It is likely that during this transition the $3R^-_d$ is transformed
647 into the $1M$ structure (with 10% residual $3R^-_h$) whereas the accessory $3R^+_d/3R^-_d$ MLS (ratio
648 70:30) from sample 350-KBi will contribute to the quasi-turbostratic phase which contains
649 $3R^-_h$ and $1M$ fragments (4:1 ratio) in sample AfterT-KBi.

650 *Origin of 1M Layers.* Because of its prevalence, the transition from the $3R^-_d$ polytype to
651 the $1M$ polytype will be considered first. As mentioned above, the new-formed Mn^{3+} -
652 octahedra in the $3R^-_d$ structure have a random orientation of their long Mn^{3+} -O bonds relative
653 to the **a** axis ($\pm n120^\circ$) thus inducing significant lattice strains in the layers. Besides, interlayer
654 K^+ cations are shifted towards the center of interlayer prismatic cavities to ensure proper
655 bond lengths with closest O_{layer} from adjacent layers. This shift, along with the absence of
656 vacant layer sites and the interlayer collapse due to dehydration, significantly increase the
657 repulsion between interlayer K^+ and Mn_{layer} . At $350^\circ C$, the effect of these structural features
658 unfavorable to layer stability is compensated for by thermal energy. Logically, when
659 lowering the temperature, stabilization of the resulting $1M$ structure will ideally lead to the
660 minimization of lattice strains and K^+ - Mn_{layer} interactions. In addition, rehydration of $1M$
661 interlayers should be accompanied by the formation of appropriate K^+ - H_2O and H_2O - O_{layer}
662 bond lengths so as to provide local charge compensation and to contribute to the cohesion
663 between adjacent layers. These different aspects of AfterT-KBi structure will be discussed
664 hereafter for the main $1M/3R^-_h$ phase.

665 From chemical analysis, sample AfterT-KBi contains ~22% of the Mn^{3+} (structural
666 formula – eq 3), and both the orthogonal symmetry of the layers in the $1M$ polytype (Table 1)
667 and the structure model determined (Table 3) suggest that these cations are actually located in

668 the octahedral layer. The presence of a significant amount of Mn^{3+} cations in vacancy-free
669 layers indeed leads, at room temperature, to the departure from the hexagonal layer symmetry
670 because of cooperative Jahn-Teller effect. The transformation of $3R_d$ polytype to $1M$
671 polytype is most likely accompanied by such re-orientation of the layer Mn^{3+} -octahedra
672 leading to a unique orientation of the long Mn^{3+} -O bonds and thus giving rise to the
673 orthogonal layer symmetry. Such systematic orientation along the **a** axis of the long Mn^{3+} -O
674 bonds of distorted octahedra minimizes strains in the layers as the four short Mn^{3+} -O
675 distances are similar to $\langle \text{Mn}^{4+}\text{-O} \rangle$ (1.93 Å vs 1.91 Å). For this reason unit-cell *b* parameters
676 are very similar (2.84-2.86 Å) in all Mn^{3+} -rich natural and synthetic varieties having
677 orthogonal layer symmetry regardless of their layer Mn^{3+} content.^{69,75,77,83,84,95} In contrast, the
678 unit-cell *a* parameter strongly depends on this content and *a/b* ratios vary significantly for
679 such Mn^{3+} -rich compounds. Values reported in the literature for *a/b* ratio are 1.936 in
680 crednerite (CuMnO_2 , $\text{Mn}^{3+} = 100\%$),⁸⁶ 1.830 in Na-buserite (NaBu , $\text{Mn}^{3+} = 33\%$, *a* =
681 5.223 Å, *b* = 2.854 Å),⁷⁵ 1.817 Å in triclinic Na-birnessite (NaBi , $\text{Mn}^{3+} = 30\%$, *a* = 5.174 Å,
682 *b* = 2.848 Å),^{77,83} and 1.811 in K-rich birnessite obtained from the thermal decomposition of
683 KMnO_4 at 1000°C (KBi_{100} , $\text{Mn}^{3+} = 25\%$, *a* = 5.155 Å, *b* = 2.846 Å).⁸⁴ In $1M$ layers of sample
684 AfterT-KBi, unit-cell *b* parameter (*b* = 2.850 Å) is consistent with literature data and *a/b* ratio
685 equals 1.800, which would correspond to ~20% of Mn^{3+} in the layers. This value is consistent
686 with the average oxidation state of Mn measured globally for sample AfterT-KBi (22%).

687 Along with the re-orientation of distorted layer Mn^{3+} -octahedra, the $3R_d$ -to- $1M$
688 transformation during cooling is accompanied by modification of layer stacking, as the
689 interlayer shift decreases from $-0.333 a$ to $-0.260 a$ ($\Delta = +0.073 a$). As the average CSDS
690 along the **c*** axis of both 350-KBi and AfterT-KBi samples is equal to 6 layers, maximum
691 displacement between layers of a given crystal induced by the layer stacking modification
692 does not exceed 5Δ , that is ~1.5 Å, taking into account the variation of unit-cell parameters.
693 This displacement is likely even smaller as hydration of the $3R_d$ interlayers during cooling

694 most likely starts simultaneously from both ends of crystals. These limited layers
695 displacements are likely to require little energy to proceed.

696 In addition, mutual arrangement of layers in the $1M$ polytype is favorable to the layer
697 stacking stability as it allows for the formation of H-bonds and for the minimization of cation
698 electrostatic repulsion. Each interlayer K^+ cation is indeed coordinated by the two nearest
699 O_{layer} from adjacent layers (2.703-2.831 Å) and by four (or even six) H_2O molecules at 2.713-
700 2.862 Å (and 3.161 Å). H_2O molecules are located at 2.616 Å from the nearest O_{layer} , thus
701 forming strong H-bonds (Figure 12). Finally, as compared to the $3R_h$ phase, the $1M$ layer
702 stacking leads to an increased K-Mn distance thus decreasing the repulsion between these
703 two cations (Figures 6 and 12).

704 Note that the main structural features of the $1M$ phase are similar to those of the K-
705 saturated birnessite synthesized at high pH and room temperature from Mn^{2+} precursors.⁸³ It
706 is likely that $3R_h$ layer fragments (10%) coexisting with the prevailing $1M$ fragments are
707 inherited from the initial $3R_d$ structure of sample 350-KBi in which the random orientation of
708 the layer Mn^{3+} octahedral is maintained.

709 *Origin of the $3R_h$ Fragments in the Quasi-Turbostratic Phase.* At first sight the
710 hypothesized transition from the $3R^+_d/3R^-_d$ MLS into the poorly crystallized phase during
711 cooling of sample 350-KBi appears unlikely as at least one of the stability unfavorable factors
712 described for the $3R^-_d$ polytype is absent in the $3R^+_d$ one. In the $3R^+_d$ phase each interlayer K^+
713 cation is indeed octahedrally coordinated and located above/below empty tridentate cavities
714 from the two neighboring layers (Figure 10). As a result, proper K- O_{layer} bond lengths are
715 obtained with closest O_{layer} from adjacent layers (Table 4), and direct interaction with the
716 Mn_{layer} cations is avoided. After cooling of the $3R^+_d/3R^-_d$ adjacent layers in the hydrated phase
717 could thus logically maintain the $+a/3$ interlayer shift along the **a** axis to preserve such
718 favorable disposition of layer and interlayer cations. In addition, this layer stacking mode
719 would allow for the formation of strong H-bonds between O_{layer} and H_2O molecules if the

720 latter were located between O_{layer} of adjacent layers in a position equivalent to (0.167, 0,
721 0.167) (Figure 10). However, through H-bonds neutral H_2O molecules provide O_{layer} with
722 positive charges and they should thus interact with interlayer cations to compensate for this
723 transfer of charge. A careful analysis of the $3R^+_h$ interlayer space shows that the location of
724 K^+ cations in the interlayer octahedral site is inconsistent with positions of H_2O molecules
725 allowing for H-bond formation, K- H_2O distances being either too short or too long. As a
726 consequence, hydration of the $3R^+_d$ phase following the cooling of sample 350-KBi should
727 involve a modification of the $3R^+$ stacking so that two conditions are satisfied. First, H_2O
728 molecules should form H-bonds with adjacent O_{layer} and interact with interlayer K^+ cations.
729 Second, interlayer K^+ cations should have appropriate coordination and proper $\langle K-O_{\text{layer}} \rangle$
730 bond length.

731 As discussed above, these two conditions are satisfied in the $1M$ phase. It is thus likely
732 that $3R^+_d$ fragments present in the $3R^+_d/3R^-_d$ MLS tend to transform into such $1M$ fragments.
733 However, thermal energy is likely not sufficient to allow a complete modification of the layer
734 stacking from $+a/3$ to $-0.260a$ and random stacking faults in the quasi-turbostratic phase
735 most likely result from displacements between adjacent layers intermediate between these
736 two values. Thermal energy is not sufficient either to modify the hexagonal layer symmetry
737 which is preserved in the quasi-turbostratic phase in spite of the unfavorable lattice constraints
738 resulting from the presence of layer Mn^{3+} cations. Note also that the relative proportion of
739 $3R^-_h$ and $1M$ fragments in the quasi-turbostratic phase (20% and 5%, respectively) is similar
740 to that of the $3R^-_d$ fragments (30%), which have the “right” interlayer displacement, in the
741 $3R^+_d/3R^-_d$ MLS in sample 350-KBi.

742 Interlayer structure of the $3R^-_h$ phase in KBi sample after cooling is similar to that
743 determined before thermal treatment. In both cases, interlayer K^+ cations are coordinated by
744 four O_{layer} defining the faces of the prism and by two H_2O molecules located in the interlayer
745 mid-plane. These H_2O molecules have appropriate distances both with the nearest O_{layer} from

746 adjacent layers and with the nearest interlayer K^+ cations. The main difference between the
747 $3R_h$ phases in KBi samples before thermal treatment and after cooling arises from their
748 respective layer cation composition. After cooling, layers of the $3R_h$ phase are vacancy-free
749 and interlayer K^+ cation are systematically located above or below Mn_{layer} . As a result, $3R_h$
750 structural fragments in AfterT-KBi sample should be considered as metastable although
751 electrostatic repulsion between the two cations is partly decreased by the shift of the
752 interlayer K^+ cations from the center of the prismatic cavity towards its faces. Metastability
753 of these fragments also comes from the presence of lattice strains originating from the
754 random orientation of distorted Mn^{3+} -octahedra in the layers.

755

756 **Acknowledgments.** VAD is grateful to the Environmental Geochemistry Group of the
757 LGIT (Grenoble, France) and to the Russian Science Foundation for financial support. BL
758 acknowledges financial support from INSU/Géomatériaux, and CNRS/PICS709 programs.
759 The authors are grateful to Pr. Alain Plançon (IST – Orléans) for the availability and the
760 modification of his XRD calculation program. Céline Boissard (Hydr'ASA – Poitiers),
761 Martine Musso and Delphine Tisserand (LGIT – Grenoble), and Serge Nitsche (CRMCN –
762 Marseilles) are thanked for their technical support (DT-TG analyses, chemical analyses, and
763 SEM images, respectively).

764

765 **References cited**

766

- 767 (1) Giovanoli, R.; Stähli, E; Feitknecht, W. *Helv. Chim. Acta* **1970**, *53*, 209-220.
- 768 (2) Giovanoli, R.; Stähli, E; Feitknecht, W. *Helv. Chim. Acta* **1970**, *53*, 453-464.
- 769 (3) Burns, R.G.; Burns, V.M. *Phil Trans Roy Soc London A* **1977**, *286*, 283-301.
- 770 (4) Glover, E.D. *Amer. Mineral.* **1977**, *62*, 278-285.

- 771 (5) Chukhrov, F.V.; Gorschkov, A.I.; Rudnitskaya, E.S.; Sivtsov, A.V. *Izv. Akad. Nauk*
772 *Geol.* **1978**, *9*, 67-76.
- 773 (6) Burns, V.M.; Burns, R.G. *Earth Planet. Sci. Lett.* **1978**, *39*, 341-348.
- 774 (7) Golden, D.C.; Dixon, J.B.; Chen, C.C. *Clays & Clay Miner.* **1986**, *34*, 511-520.
- 775 (8) Chukhrov, F.V.; Sakharov, B.A.; Gorshkov, A.I.; Drits, V.A.; Dikov, Yu.P. *Int. Geol.*
776 *Rev.* **1985**, *27*, 1082-1088.
- 777 (9) Drits, V.A.; Petrova, V.V.; Gorshkov, A.I. *Lithology and Raw Materials* **1985**, *3*, 17-
778 39.
- 779 (10) Cornell, R.M.; Giovanoli, R. *Clays & Clay Miner.* **1988**, *36*, 249-257.
- 780 (11) Manceau, A.; Lanson, B.; Schlegel, M. L.; Harge, J. C.; Musso, M.; Eybert Berard,
781 L.; Hazemann, J. L.; Chateigner, D.; Lambelle, G. M. *Amer. J. Sci.* **2000**, *300*, 289-343.
- 782 (12) Bilinski, H.; Giovanoli, R.; Usui, A.; Hanzel, D. *Amer. Mineral.* **2002**, *87*, 580-591.
- 783 (13) Rogers, T. D. S.; Hodkinson, R. A.; Cronan, D. S. *Marine Georesources and*
784 *Geotechnology* **2001**, *19*, 245-268.
- 785 (14) McKeown, D. A.; Post, J. E. *Amer. Mineral.* **2001**, *86*, 701-713.
- 786 (15) Exon, N. F.; Raven, M. D.; De Carlo, E. H. *Marine Georesources and Geotechnology*
787 **2002**, *20*, 275-297.
- 788 (16) Mote, T. I.; Becker, T. A.; Renne, P.; Brimhall, G. H. *Econ. Geol. Bull. Soc. Econ.*
789 *Geol.* **2001**, *96*, 351-366.
- 790 (17) Morozov, A. A.; Novikov, G. V.; Kulikova, L. N. *Geochemistry International* **2001**,
791 *39*, 764-779.
- 792 (18) Manceau, A.; Tamura, N.; Celestre, R. S.; MacDowell, A. A.; Geoffroy, N.; Sposito,
793 G.; Padmore, H. A. *Environ. Sci. Technol.* **2003**, *37*, 75-80.
- 794 (19) Vaniman, D. T.; Chipera, S. J.; Bish, D. L.; Duff, M. C.; Hunter, D. B. *Geochim.*
795 *Cosmochim. Acta* **2002**, *66*, 1349-1374.
- 796 (20) Chao, T. T.; Theobald, P. K. *Econ. Geol.* **1976**, *71*, 1560-1569.

- 797 (21) Manceau, A.; Drits, V.A.; Silvester, E.J.; Bartoli, C.; Lanson, B. *Amer. Mineral.* **1997**,
798 82, 1150-1175.
- 799 (22) Manceau, A.; Schlegel, M. L.; Chateigner, D.; Lanson, B.; Bartoli, C.; Gates, W. P. In
800 *Synchrotron X-ray methods in clay science*; Schulze, D. G., Stucki, J. W., Bertsch, P. M.,
801 Eds.; Clay Minerals Society: Boulder, Co, 1999; Clay Miner. Soc. Workshop Lectures Vol. 9,
802 pp 68-114.
- 803 (23) Manceau, A.; Lanson, B.; Drits, V. A.; Chateigner, D.; Gates, W. P.; Wu, J.; Huo, D.;
804 Stucki, J. W. *Amer. Mineral.* **2000**, 85, 133-152.
- 805 (24) Manceau, A.; Drits, V. A.; Lanson, B.; Chateigner, D.; Wu, J.; Huo, D.; Gates, W. P.;
806 Stucki, J. W. *Amer. Mineral.* **2000**, 85, 153-172.
- 807 (25) Taylor, R.M.; McKenzie, R.M.; Norrish, K. *Aust. J. Soil Res.* **1964**, 2, 235-248.
- 808 (26) McKenzie, R.M. *Aust. J. Soil Res.* **1967**, 5, 235-246.
- 809 (27) McKenzie, R.M. *Aust. J. Soil Res.* **1980**, 18, 61-73.
- 810 (28) Kim, J. G.; Dixon, J. B.; Chusuei, C. C.; Deng, Y. *J. Soil Sci. Soc. Am. J.* **2002**, 66,
811 306-315.
- 812 (29) Cheney, M. A.; Shin, J. Y.; Crowley, D. E.; Alvey, S.; Malengreau, N.; Sposito, G.
813 *Colloid Surface A* **1998**, 137, 267-273.
- 814 (30) Mench, M. J.; Manceau, A.; Vangronsveld, J.; Clijsters, H.; Mocquot, B. *Agronomie*
815 **2000**, 20, 383-397.
- 816 (31) McBride, M. B.; Martinez, C. E. *Environ. Sci. Technol.* **2000**, 34, 4386-4391.
- 817 (32) Healy, T.W.; Herring, A.P.; Fuerstenau, D.W. *J. Colloid Interface Sci.* **1966**, 21, 435-
818 444.
- 819 (33) Balistrieri, L.S.; Murray, J.W. *Geochim. Cosmochim. Acta* **1982**, 46, 1041-1052.
- 820 (34) Gray, MJ; Malati, MA. *J. Chem. Technol. Biotechnol.* **1979**, 29, 127-134.
- 821 (35) Stumm, W. *Chemistry of the solid-water interface and particle-water interface in*
822 *natural systems*; Wiley: New York, 1992.

- 823 (36) Le Goff, P.; Baffier, N.; Bach, S.; Pereira-Ramos, J-P. *Mat. Res. Bull.* **1996**, *31*, 63-
824 75.
- 825 (37) Tu, S.; Racz, G.J.; Goh, T.B. *Clays & Clay Miner.* **1994**, *42*, 321-330.
- 826 (38) Paterson, E.; Swaffield, R.; Clark, L. *Clay Miner.* **1994**, *29*, 215-222.
- 827 (39) Novikov, G. V.; Cherkashev, G. A. *Geochemistry International* **2000**, *38 Suppl. 2*,
828 S194-S205.
- 829 (40) Dyer, A.; Pillinger, M.; Harjula, R.; Amin, S. *J. Mater. Chem.* **2000**, *10*, 1867-1874.
- 830 (41) Naidja, A.; Liu, C.; Huang, P. M. *J. Colloid Interface Sci.* **2002**, *251*, 46-56.
- 831 (42) Gray, MJ; Malati, MA. *J. Chem. Technol. Biotechnol.* **1979**, *29*, 135-144.
- 832 (43) Catts, J.G.; Langmuir, D. *Appl. Geochem.* **1986**, *1*, 255-264.
- 833 (44) Ran, Y.; Fu, J. M.; Rate, A. W.; Gilkes, R. J. *Chem. Geol.* **2002**, *185*, 33-49.
- 834 (45) Manceau, A.; Gorshkov, A.I.; Drits, V.A. *Amer. Mineral.* **1992**, *77*, 1144-1157.
- 835 (46) Manceau, A.; Gorshkov, A.I.; Drits, V.A. *Amer. Mineral.* **1992**, *77*, 1133-1143.
- 836 (47) Silvester, E.J.; Manceau, A.; Drits, V.A. *Amer. Mineral.* **1997**, *82*, 962-978.
- 837 (48) Manceau, A.; Charlet, L. *J. Colloid Interface Sci.* **1992**, *148*, 425-442.
- 838 (49) Stone, A.T.; Godtfredsen, K.L.; Deng, B. In *Chemistry of aquatic systems: Local and*
839 *global perspectives*; Bidoglio, G., Stumm, W., Eds.; ECSC, EEC, EAEC: Brussels, 1994, pp
840 337-374.
- 841 (50) Guha, H.; Saiers, J. E.; Brooks, S.; Jardine, P.; Jayachandran, K. *Journal of*
842 *Contaminant Hydrology* **2001**, *49*, 311-334.
- 843 (51) Tournassat, C.; Charlet, L.; Bosbach, D.; Manceau, A. *Environ. Sci. Technol.* **2002**,
844 *36*, 493-500.
- 845 (52) Petrie, R. A.; Grossl, P. R.; Sims, R. C. *Environ. Sci. Technol.* **2002**, *36*, 3744-3748.
- 846 (53) Manning, B. A.; Fendorf, S. E.; Bostick, B.; Suarez, D. L. *Environ. Sci. Technol.*
847 **2002**, *36*, 976-981.
- 848 (54) Banerjee, D.; Nesbitt, H. W. *Geochim. Cosmochim. Acta* **1999**, *63*, 1671-1687.

- 849 (55) Kim, S. H.; Im, W. M.; Hong, J. K.; Oh, S. M. *J. Electrochem. Soc.* **2000**, *147*, 413-
850 419.
- 851 (56) Feng, Q; Kanoh, H; Miyai, Y; Ooi, K. *Chem. Mater.* **1995**, *7*, 1226-1232.
- 852 (57) Chen, R.J.; Zavalij, P; Whittingham, M.S. *Chem. Mater.* **1996**, *8*, 1275-1280.
- 853 (58) Chen, R.J.; Chirayil, T.; Zavalij, P.; Whittingham, M.S. *Solid State Ionics* **1996**, *86*-
854 *88*, 1-7.
- 855 (59) Bach, S; Henry, M; Baffier, N; Livage, J. *J. Solid State Chem.* **1990**, *88*, 325-333.
- 856 (60) Bach, S; Pereira-Ramos, J-P; Bafier, N. *Electrochim. Acta* **1993**, *38*, 1695-1698.
- 857 (61) Le Goff, P; Baffier, N; Bach, S; Pereira-Ramos, J-P. *J. Mater. Chem.* **1994**, *4*, 875-
858 881.
- 859 (62) Ching, S.; Landrigan, J.A.; Jorgensen, M.L.; Duan, N.; Suib, S.L.; O'Young, C.L.
860 *Chem. Mater.* **1995**, *7*, 1604-1606.
- 861 (63) Ching, S; Petrovay, D J; Jorgensen, M L; Suib, S L. *Inorg. Chem.* **1997**, *36*, 883-890.
- 862 (64) Cho, J; Kim, G B; Lim, H S; Kim, C-S; Yoo, S-I. *Electrochemical and Solid-State*
863 *Letters* **1999**, *2*, 607-609.
- 864 (65) Tsuji, M.; Komarneni, S.; Tamaura, Y.; Abe, M. *Mat. Res. Bull.* **1992**, *27*, 741-751.
- 865 (66) Leroux, F; Guyomard, D; Piffard, Y. *Solid State Ionics* **1995**, *80*, 299-306.
- 866 (67) McKenzie, R.M. *Miner. Mag.* **1971**, *38*, 493-502.
- 867 (68) Herbstein, H.F.; Ron, G.; Weissman, A. *J. Chem. Soc. (A)* **1971**, 1821-1826.
- 868 (69) Kim, S. H.; Kim, S. J.; Oh, S. M. *Chem. Mater.* **1999**, *11*, 557-563.
- 869 (70) Gaillot, A. C.; Flot, D.; Drits, V. A.; Manceau, A.; Burghammer, M.; Lanson, B.
870 *Chem. Mater.* **2003**, *15*, 4666-4678.
- 871 (71) Gaillot, A-C; Lanson, Bruno.; Drits, V A. *Chem. Mater.* **2005**, *in preparation*.
- 872 (72) Vetter, K J; Jaeger, N. *Electrochim. Acta* **1966**, *11*, 401-419.
- 873 (73) Lingane, J J; Karplus, R. *Ind. Eng. Chem. Anal. Ed.* **1946**, *18*, 191-194.

- 874 (74) Drits, V.A.; Tchoubar, C. *X-ray diffraction by disordered lamellar structures: Theory*
875 *and applications to microdivided silicates and carbons*; Springer-Verlag: Berlin, 1990.
- 876 (75) Drits, V. A.; Lanson, B.; Gorshkov, A. I.; Manceau, A. *Amer. Mineral.* **1998**, *83*, 97-
877 118.
- 878 (76) Lanson, B.; Drits, V.A.; Silvester, E.J.; Manceau, A. *Amer. Mineral.* **2000**, *85*, 826-
879 838.
- 880 (77) Lanson, B.; Drits, V. A.; Feng, Q.; Manceau, A. *Amer. Mineral.* **2002**, *87*, 1662-1671.
- 881 (78) Lanson, B.; Drits, V. A.; Gaillot, A. C.; Silvester, E.; Plançon, A.; Manceau, A. *Amer.*
882 *Mineral.* **2002**, *87*, 1631-1645.
- 883 (79) Gaillot, A. C.; Drits, V. A.; Plançon, A.; Lanson, B. *Chem. Mater.* **2004**, *16*, 1890-
884 1905.
- 885 (80) Plançon, A., Ph. D. Thesis, Orléans, France, 1976.
- 886 (81) Plançon, A. *J. Appl. Cryst.* **2002**, *35*, 377.
- 887 (82) Wang, Z L; Yin, J S; Jiang, Y D. *Micron* **2000**, *31*, 571-580.
- 888 (83) Post, J.E.; Veblen, D.R. *Amer. Mineral.* **1990**, *75*, 477-489.
- 889 (84) Gaillot, A.-C.; Drits, V.A.; Lanson, B.; Manceau, A. *Chem. Mater.* **2005**, *In*
890 *preparation*.
- 891 (85) Thackeray, M.M.; de Kock, A.; David, W.I.F. *Mat. Res. Bull.* **1993**, *28*, 1041-1049.
- 892 (86) Töpfer, J.; Trari, M.; Gravereau, P.; Chaminade, J.P.; Doumerc, J.P. *Z. Kristallogr.*
893 **1995**, *210*, 184-187.
- 894 (87) Shannon, R.D.; Gumeman, P.S.; Chenavas, J. *Amer. Mineral.* **1975**, *60*, 714-716.
- 895 (88) Glasser, L.S.D.; Ingram, L. *Acta Crystallogr.* **1968**, *B24*, 1233-1236.
- 896 (89) Dachs, H. *Z. Kristallogr.* **1963**, *118*, 303-326.
- 897 (90) Drits, V.A.; McCarty, D.K. *Amer. Mineral.* **1996**, *81*, 852-863.
- 898 (91) Drits, V.A.; Varaxina, T.V.; Sakharov, B.A.; Plançon, A. *Clays & Clay Miner.* **1994**,
899 *42*, 382-390.

- 900 (92) Méring, J. *Acta Crystallogr.* **1949**, 2, 371-377.
- 901 (93) Villalobos, M.; Lanson, B.; Manceau, A.; Toner, B.; Sposito, G. *Amer. Mineral.* **2005**,
- 902 submitted.
- 903 (94) Post, J.E.; Appleman, D.E. *Amer. Mineral.* **1988**, 73, 1401-1404.
- 904 (95) Drits, V.A.; Silvester, E.J.; Gorshkov, A.I.; Manceau, A. *Amer. Mineral.* **1997**, 82,
- 905 946-961.
- 906 (96) Muller, F.; Drits, V. A.; Plancon, A.; Besson, G. *Clay Miner.* **2000**, 35, 491-504.
- 907 (97) Muller, F.; Drits, V. A.; Tsipursky, S. I.; Plancon, A. *Clay Miner.* **2000**, 35, 505-514.
- 908 (98) Muller, F.; Drits, V.; Plancon, A.; Robert, J. L. *Clays & Clay Miner.* **2000**, 48, 572-
- 909 585.

910

911

Figure captions

912

913 **Figure 1.** Scanning electron micrographs of KBi particles

914 **Figure 2.** Experimental TD-TG and DSC curves obtained for samples RoomT-KBi (a) and
915 AfterT-KBi (b). The different endothermal peaks corresponding to successive loss of weight
916 occur at ~90°C, ~140°C, 250-400°C, and ~890°C and are labeled a, b, c, and d, respectively
917 for sample RoomT-KBi. For sample AfterT-KBi a weight gain rather than a weight loss is
918 observed over the 250-400°C temperature interval.

919 **Figure 3.** Experimental powder XRD pattern obtained for KBi samples. (a) Pattern recorded
920 at room temperature (sample RoomT-KBi). (b) to (e) Patterns recorded *in situ* at 100°C,
921 150°C, 250°C and 350°C (samples 100-, 150-, 250- and 350-KBi, respectively). (f) Pattern
922 recorded after the complete thermal treatment up to 350°C and subsequent cooling to room
923 temperature (sample AfterT-KBi).

924 **Figure 4.** Evolution of unit-cell parameters for KBi samples as a function of temperature.
925 The solid and dashed lines outline the variation of unit-cell parameters in the main ordered
926 structure, and in the accessory structures, respectively.

927 **Figure 5.** (a) Comparison of calculated XRD patterns corresponding to the $3R^+$ (solid line)
928 and $3R^-$ (crosses) polytypes. (b) to (d) Comparison between experimental (crosses) and
929 calculated (solid line) XRD patterns for sample RoomT-KBi. (b) Calculation performed
930 assuming a periodic $3R^-$ polytype ($R_{wp} = 15.77\%$). Arrows indicate the misfits at peak tails.
931 (c) Calculation performed assuming a quasi-turbostratic phase with small coherent scattering
932 domain size. (d) Optimum model. The calculated pattern is the sum of the periodic $3R^-$
933 polytype and of the quasi-turbostratic phase ($R_{wp} = 9.55\%$).

934 **Figure 6.** Structure model for the $3R^-$ polytype. (a) Projection on the **ab** plane. The upper
935 surface of the lower layer is shown as light shaded triangles whereas the lower surface of the
936 upper layer is shown as dark shaded triangles. Mn_{layer} and O_{layer} of the two layers are shown
937 as small and big solid circles, respectively. Large shaded circles represent interlayer K^+ .
938 Position 1 corresponds to the faces of the interlayer prism defined by two empty tridentate
939 layer cavities, whereas position 2 corresponds to the center of this prism. Position 3
940 corresponds to the optimum model. Open circles with a dashed outline (position 4) represent
941 H_2O molecules. Dot-dashed lines outline the coordination polyhedron of interlayer K^+ cations
942 which includes 4 O_{layer} and 2 H_2O molecules. (b) Projection along the **b** axis. Open and solid
943 symbols indicate atoms at $y = 0$ and $y = \pm 1/2$, respectively. Large circles represent O_{layer} atoms,
944 small circles represent Mn_{layer} atoms, and squares represent vacant layer octahedra. Dot-
945 dashed lines outline the interlayer prisms defined by two empty tridentate layer cavities. The
946 center of these prisms is shown by regular dashed lines. Other patterns as in Figure 6a.

947 **Figure 7.** Comparison between experimental (crosses) and calculated (lines) XRD patterns
948 for sample RoomT-KBi. Comparison is shown for $20\ell/11\ell$ reflections (a) and for $31\ell/02\ell$
949 ones (b). Dot-dashed and dashed lines correspond to calculations performed assuming

950 interlayer K^+ cations on the faces (position 1 in Figure 6) or in the center (position 2 in Figure
951 6) of the interlayer prism, respectively. The solid line corresponds to the calculation
952 performed with the optimum position of interlayer K^+ cations (position 3 in Figure 6).

953 **Figure 8.** Comparison between experimental (crosses) and calculated (solid line) XRD
954 patterns for KBi samples. (a) Sample 100-KBi. Calculation performed for a periodic hydrated
955 $3R^-$ polytype ($R_{wp} = 18.59\%$). (b) Sample 100-KBi. Calculation performed for a mixed-layer
956 structure in which 70% of the layers are dehydrated. (c) Sample 100-KBi. Optimum model.
957 The calculated pattern is the sum of a periodic hydrated $3R^-$ polytype, of a mixed-layer
958 structure in which 70% of the layers are dehydrated and of a quasi-turbostratic phase ($R_{wp} =$
959 12.24%). (d) Sample 150-KBi. Optimum model. The calculated pattern is the sum of a
960 periodic dehydrated $3R^-$ polytype and of a quasi-turbostratic phase ($R_{wp} = 8.92\%$). (e) Sample
961 250-KBi Optimum model. The calculated pattern is the sum of a periodic dehydrated $3R^-$
962 polytype and of a quasi-turbostratic phase ($R_{wp} = 9.97\%$)

963 **Figure 9.** Comparison between experimental (crosses) and calculated (solid line) XRD
964 patterns for sample 350-KBi. (a) Calculation performed for a periodic $3R^-$ polytype. (b)
965 Calculation performed for a mixed-layer structure containing 30% of layers shifted by $-a/3$
966 along the **a** axis ($3R^-$ fragments) and 70% of layers shifted by $+a/3$ along the **a** axis ($3R^+$
967 fragments). (c) Optimum model. The calculated pattern is the sum of a quasi-periodic $3R^-$
968 structure of the above $3R^-/3R^+$ mixed-layer structure, and of a quasi-turbostratic structure
969 ($R_{wp} = 9.92\%$).

970 **Figure 10.** Structure model for the $3R^+$ polytype (a) Projection on the **ab** plane. (b) Projection
971 along the **b** axis. Patterns as in Figure 6.

972 **Figure 11.** Comparison between experimental (crosses) and calculated (solid line) XRD
973 patterns for sample AfterT-KBi. (a) Calculation performed for a mixed-layer structure
974 containing $1M$ and $3R^-$ structural fragments (90:10 ratio – $R_{wp} = 23.03\%$). (b) Calculation
975 performed for a quasi-turbostratic phase containing $3R^-$ and $1M$ structural fragments. (c)

976 Optimum model. The calculated pattern is the sum of the $1M/3R$ mixed-layer structure and
977 of the quasi-turbostratic structure described above ($R_{wp} = 8.67\%$).

978 **Figure 12.** Structure model for the $1M$ polytype. (a) Projection on the **ab** plane. (b)
979 Projection along the **b** axis. Patterns as in Figure 6.

980

Table 1. Unit-cell parameters of KBi samples as a function of temperature

	Polytype	a ^a	b ^a	c ^a	β
RoomT-KBi	$3R^-$	4.928	2.845	21.492	90°
100-KBi	$3R^-$	4.928	2.845	21.120 19.380	90°
150-KBi	$3R^-$	4.936	2.850	19.380	90°
250-KBi	$3R^-$	4.938	2.851	19.260	90°
350-KBi	$3R^-$ ^b	4.967	2.868	19.206	90°
	$3R^-/3R^+$ ^c	4.997	2.885	19.356	
AfterT-KBi	$3R^-$ ^d	4.971	2.870	21.150	90°
	$1M$	5.130	2.850	7.126	100.8°

^a Unit-cell parameters are given in Å. ^b Unit-cell parameters of the main quasi-periodic phase. ^c Unit-cell parameters of the $3R^+/3R^-$ mixed layer phase. ^d Unit-cell parameters of the $3R^-$ fragments in both the main phase and in the quasi-turbostratic phase

Table 2. Indexing of the Experimental XRD Patterns of KBi Samples with $3R$ and $1M$ Unit Cells.

$3R$	Room T		100-KBi		150-KBi		250-KBi		350-KBi		AfterT-KBi		$1M$
	$hk\ell^a$	d_{exp}^b	d_{calc}^c	d_{exp}	d_{calc}	d_{exp}	d_{calc}	d_{exp}	d_{calc}	d_{exp}	d_{calc}	d_{exp}	
003	7.167	7.164	7.039	7.040	6.494	6.468	6.468	6.420	6.437	6.442	7.063	7.000	001
006	3.581	3.582	3.524	3.520	3.234	3.234	3.222	3.210	3.220	3.221	3.529	3.500	002
											2.523	2.526	20-1
												2.520	200
201	2.446	2.445	2.447	2.445	2.446	2.445	2.449	2.447	2.457	2.465	2.476	2.481	110
112	2.399	2.399	2.398	2.399	2.390	2.391	2.390	2.390	2.404	2.404	2.410	2.409	11-1
009		2.388		2.347		2.156		2.140		2.147	2.351	2.333	003
204	–	2.237	2.227	2.231		2.197	–	2.195	2.200	2.210	2.245	2.255	20-2
											2.241	2.201	201
115	2.136	2.136	2.126	2.128	2.083	2.082	2.080	2.078	2.096	2.089	2.131	2.118	11-2
											2.117	1.941	112
											1.962		
207	1.919	1.920	1.906	1.908	1.834	1.842	1.832	1.837	1.839	1.847	1.910	1.898	20-3
118	1.814	1.815	1.797	1.801	1.726	1.730	1.724	1.723	1.736	1.731	1.795	1.784	11-3
00.12	1.791	1.791	1.765	1.760	1.615	1.617	1.607	1.605	1.614	1.611		1.750	004
20.10	1.615	1.619	1.601	1.603	1.521	1.525	1.514	1.518	1.520	1.526	1.614	1.626	113
											1.567	1.571	203
11.11	1.530	1.530	1.515	1.514		1.435	1.437	1.428	1.436	1.434	1.485	1.465	31-1
											1.449	1.447	310
310	1.421	1.421	1.421	1.422	1.422	1.423	1.423	1.424	1.436	1.434	1.422	1.425	020
020												1.421	31-2
313	1.395	1.394	1.394	1.394	1.390	1.390	1.392	1.390	1.403	1.400	1.395	1.396	021
023													
20.13	1.374	1.372	1.363	1.356	1.300	1.294	1.270	1.270	1.319	1.276	1.374	1.374	311
316	1.322	1.321	1.321	1.318	1.300	1.303	1.308	1.302	1.287	1.310	1.328	1.330	31-3
026													
319	1.224	1.221	1.222	1.221	1.223	1.234	1.221	1.221	1.187	1.221	1.239	1.240	220
029													

^a All KBi samples are indexed as $3R$ polytypes (indices in the left-hand side column), except for sample AfterT-KBi which is indexed as a $1M$ polytype (indices in the right-hand side column). ^b $d_{\text{exp}}(hk\ell)$ are measured experimentally. ^c $d_{\text{calc}}(hk\ell)$ values are calculated using the unit-cell parameters of the main phases listed in Table 1.

Table 3. Atomic positions, sites occupancies and other structural parameters in hydrothermal KBi samples

		RoomT- KBi	100-KBi	150-KBi	250-KBi	350-KBi		AfterT-KBi	
		$3R^-$	$3R^-$	$3R^-$	$3R^-$	A layer, $3R^-$	B layer, $3R^+$	$3R^-$	$1M^a$
Mn	x^a	0	0	0	0	0	0	0	0
	y^a	0	0	0	0	0	0	0	0
	z	0	0	0	0	0	0	0	0
	occ	0.925	0.925	0.925	0.925	1.000	1.000	1.000	1.000
O	x^a	± 0.333	± 0.333	± 0.333	± 0.333	± 0.333	± 0.333	± 0.333	± 0.341
	y^a	0	0	0	0	0	0	0	0
	z	± 0.0465	± 0.0473	± 0.0516	± 0.0519	± 0.0516	± 0.0516	± 0.0473	± 0.143
	ζ^b	± 1.00	± 1.00	± 1.00	± 1.00	± 1.00	± 1.00	± 1.00	± 1.00
	occ	2	2	2	2	2	2	2	2
K^c	x^a	-0.240	-0.240	-0.270	-0.290	-0.300	-0.300	-0.24	-0.400
	y^a	0	0	0	0	0	0	0	0
	z	0.5	0.5	0.5	0.5	0.5	0.5	0.5	0.5
	ζ^b	3.582	3.525	3.230	3.210	3.201	3.226	3.525	3.500
	occ	0.050 x2	0.050 x2	0.050 x2	0.050 x2	0.050 x2	0.050 x2	0.050 x2	0.150 x2
K^c	x^a	0.120	0.120	0.135	0.145	0.150	0.150	0.120	–
	y^a	± 0.360	± 0.360	± 0.405	± 0.435	± 0.450	± 0.450	± 0.360	–
	z	0.5	0.5	0.5	0.5	0.5	0.5	0.5	–
	ζ^b	3.582	3.525	3.230	3.210	3.201	3.226	3.525	–
	occ	0.050 x4	0.050 x4	0.050 x4	0.050 x4	0.050 x4	0.050 x4	0.050 x4	–
H_2O^c	x^a	0.500	0.450	–	–	–	–	0.500	-0.4500
	y^a	0	0	–	–	–	–	0	0
	z	0.167	0.0167	–	–	–	–	0.167	0.5
	ζ^b	3.582	3.525	–	–	–	–	3.525	3.500
	occ	0.070 x2	0.070 x2	–	–	–	–	0.060 x2	0.190 x2
H_2O^c	x^a	-0.250	-0.225	–	–	–	–	-0.250	–
	y^a	± 0.750	± 0.675	–	–	–	–	± 0.750	–
	z	0.167	0.0167	–	–	–	–	0.167	–
	ζ^b	3.582	3.525	–	–	–	–	3.525	–
	occ	0.070 x4	0.070 x4	–	–	–	–	0.060 x4	–
N^d		6/30	6/30	6/30	6/30	6/30	6/30	–	6/30
W_R^e		5%	10-12%	12%	17%	10%	30%	–	30%
CSD ^f		350,	230	230	180	230	200	–	250

^a x and y atomic positions are expressed in fraction of unit-cell a and b parameters. x positions are given in projection normal to the \mathbf{ab} plane. ^b Position ζ along c is expressed in Å to emphasize the thickness of layer and interlayer polyhedra. ^c For K and H_2O only 3 of the 6 equivalent sites are reported. Additional sites are obtained by the symmetry operation $x = -x$ and $z = -z$. ^d The extension of the coherent scattering domains perpendicular to the layer plane is expressed in number of layers N (mean/average). ^e W_R is the occurrence probability of random stacking faults for the well-crystallized phases. ^f CSD is the radius of the coherent scattering domains in the \mathbf{ab} plane. For the quasi-turbostratic phase present in all samples, $W_R = 75\%$ and CSDS = 70 Å. The values of Debye-Waller thermal factor (B) are 0.5, 1.0, 2.0 and 2.0 for Mn_{layer} , O_{layer} , $K_{\text{interlayer}}$ and $H_2O_{\text{interlayer}}$, respectively.

Table 4. Selected inter-atomic distances (in Å) in hydrothermal KBi samples

		RoomT-KBi	100-KBi	150-KBi	250KBi	350-KBi		AfterT-KBi	
		$3R^-$	$3R^-$	$3R^-$	$3R^-$	$3R^-$	$3R^+$	$3R^-$	$1M$
Height of Mn layer		2.000	2.000	2.000	2.000	2.000	2.000	2.000	2.000
$Mn_{layer}-Mn_{layer}$	×3	2.845	2.845	2.850	2.851	2.868	2.885	2.870	2.934 ×1 2.850 ×2
$Mn_{layer}-O_{layer}$	×6	1.923	1.923	1.924	1.927	1.935	1.943	1.935	1.923 ×4 2.015 ×2
Height of interlayer		5.164	5.040	4.460	4.420	4.402	4.452	5.050	5.000
K-O short	×4	2.970	2.917	2.696	2.709	2.708	2.734	2.928	2.703 ×1
$K_{interlayer}-O_{layer}$ long	×2	3.330	3.282	2.968	2.855	2.855	2.881	3.298	2.831 ×1
Average $K_{interlayer}-O_{layer}$	×6	3.090	3.039	2.787	2.758	2.757	2.783	3.051	2.767 ×2
$K_{interlayer}-H_2O_{interlayer}$	×1	2.924	2.922	–	–	–	–	2.949	2.713 ×2
	×2	3.222	3.222	–	–	–	–	3.251	2.862 ×2 3.161 ×2
$O_{layer}-H_2O_{interlayer}$	×2	2.705	2.650	–	–	–	–	2.658	2.616 ×1 2.720 ×1
O-H ₂ O-O angle		144.71°	143.90°	–	–	–	–	143.67°	139.56

